International Journal of Plasticity 144 (2021) 103026

Contents lists available at ScienceDirect

International Journal of Plasticity

journal homepage: www.elsevier.com/locate/ijplas

Effect of neighboring grain orientation on strain localization in slip bands in HCP materials

Behnam Ahmadikia [a,*], M. Arul Kumar [b], Irene J. Beyerlein [a,c]

[a] Department of Mechanical Engineering, University of California at Santa Barbara, Santa Barbara, CA, 93106, USA
[b] Materials Science and Technology Division, Los Alamos National Laboratory, Los Alamos, NM, 87545, USA
[c] Materials Department, University of California at Santa Barbara, Santa Barbara, CA, 93106, USA

ARTICLE INFO

Keywords:
Crystal plasticity
Microstructures
Anisotropic material
Elastic-viscoplastic material
Slip transmission

ABSTRACT

Particularly in plastically anisotropic crystals, such as hexagonal close packed (HCP) materials, plastic deformation is realized by slip acting in the small volumes within individual crystals. Here we extend a full field fast Fourier transform (FFT)-based elasto-viscoplastic formulation to simulate the development of a single slip band on either prismatic or basal planes spanning a crystal. Calculations of the strain and stress fields induced locally within the band and parent crystal, and ahead of the band/grain boundary junction in the neighboring crystal are analyzed as the slip band intensifies under increasing applied strain. We report a substantial influence of the crystallographic orientation of the nearest neighboring grain on the rate of slip band localization. Performing the analysis on two materials, CP-Ti and Mg, indicates that the strength of the material affects the rate of localization, with stronger materials tending to localize more easily. A slip band tip stress-based criterion is proposed for identifying the nearest neighbor orientations in which slip band transmission is possible and the likely slip system for which it occurs. This indicator is validated against experimental studies on commercially pure Ti, an Mg–Y alloy, and Ti–6Al–4V. We show that for low GB misorientations, the slip band is likely to transmit into another slip band of the same type in the neighbor grain, while for high GB misorientations, it is likely to transmit into one of a different type or to not transmit at all.

1. Introduction

Plastic deformation in hexagonal close-packed (HCP) metals, like in many other polycrystalline materials, is commonly understood to occur heterogeneously (Akhtar and Teghtsoonian, 1971; Ardeljan et al., 2015; Barton and Dawson, 2001; Diard et al., 2005; Solas and Tomé, 2001; Wang et al., 2010). The amount of slip can vary not only among grains within the same polycrystal, but also vary significantly within an individual grain. The intragranular heterogeneity in plastic deformation can manifest in different ways, such as by slip localization in intense slip bands or kink bands, deformation twinning and lattice reorientation gradients, to name a few (Echlin et al., 2016; Hagihara et al., 2010; Lentz et al., 2016; Liu et al., 2014; Vasilev et al., 2020; Williams et al., 2002; Wronski et al., 2018).

Within a plastically strained crystal, slip occurs via dislocation glide on specific crystallographic planes, but when intense glide happens predominantly on a particular plane or closely spaced parallel planes, intense slip bands, may form. Such intense slip bands within one grain can transmit into a neighboring grain (Ding et al., 2016; Zhou et al., 2020), initiate twinning (Wang et al., 2010; Zhou

* Corresponding author.
E-mail address: behnam_ahmadikia@ucsb.edu (B. Ahmadikia).

https://doi.org/10.1016/j.ijplas.2021.103026
Received 5 October 2020; Received in revised form 24 March 2021; Accepted 5 May 2021
Available online 14 May 2021

et al., 2020), trigger a chain of bands across the polycrystal (Echlin et al., 2016), or serve as precursors for voids or cracks formation (Chan and Davidson, 1999; Zhang and Wang, 2003).

In recent years, many advanced experimental techniques have been utilized to characterize heterogeneous slip occurring in individual crystals and polycrystals. Echlin et al. (2016) utilized an *in-situ* high resolution scanning electron microscope digital image correlation (SEM DIC) technique to study the development of intense slip bands in deformed Ti–6Al–4V alloy. Slip bands formed primarily on the prismatic and basal planes and at strain levels lower than macroscopic yield strain. They showed that such bands successively transmitted from one grain to another, spanning as many as 21 grains. Using electron back-scattered diffraction (EBSD) in commercially pure titanium (CP–Ti), Wang et al. (2010) observed the formation of prismatic slip bands in the crystallographically softer grains and $\{10\bar{1}2\}\langle\bar{1}011>$ tensile twins in the neighboring grains connected to them across their grain boundaries. Localized plasticity in intense slip bands in a grain does not always transmit to slip or twinning in the neighboring grain. Guo et al. (2020) investigated the mechanisms of slip transfer in Ti through calculation of the density of geometrically necessary dislocations (GNDs) and found that when the grain neighbor does not provide an easy path for dislocation transmission, it is more likely that a dislocation pile-up forms inside the slipping grain at the grain boundary rather than slip transfers occurs at the boundary. By measuring the residual shear stress ahead of a basal slip band blocked at the grain boundary in pure magnesium, Andani et al. (2020) verified that a stress concentration at the band tip in the neighboring grain may form due to the development of slip bands in the parent grain and their interaction with the grain boundary.

Numerous studies have been carried out aiming to identify a criterion to explain slip transmission phenomenon in crystalline materials. In the beginning, the likelihood that slip transmission occurs from one slip system to another has been quantified by geometric parameters. Livingston and Chalmers (1957) were the first to consider a geometric factor,*N*, to gauge the likelihood transmission would occur between a slip system in one grain and another slip system in the neighboring grain. Their *N* is given by:

$$N = (\mathbf{n}_i.\mathbf{n}_o)\cdot(\mathbf{b}_i.\mathbf{b}_o) + (\mathbf{n}_i.\mathbf{b}_o)\cdot(\mathbf{b}_i.\mathbf{n}_o) \tag{1}$$

where the unit vectors **n** and **b** respectively represent the slip plane normal and Burgers vector (i.e., slip direction) of incoming and outgoing systems, which are denoted by the subscripts i and o, respectively. Later, Luster and Morris (1995) noted that this factor would suggest a non-intuitive transmission for two slip systems with mutually perpendicular slip directions. To circumvent this problem, they modified *N* by removing the second term in Eq. (1) and leaving the following

$$m' = (\mathbf{n}_i.\mathbf{n}_o)\cdot(\mathbf{b}_i.\mathbf{b}_o) \tag{2}$$

Attractive in its simplicity, m' has since been widely used in the literature to either anticipate or explain slip transmission. Yet still, it has not been uniformly applicable across many different conditions, such as material, slip system orientation, and grain boundary angle. In efforts to improve it, other geometric slip transmission indicators have been proposed that account for different microstructural measures, such as grain boundary orientation (Shen et al., 1986) and residual Burgers vector (Lee et al., 1989). Lee et al. (1990) conducted an *in situ* TEM analysis of the interaction of gliding dislocations with the grain boundaries in HCP metals and proposed three conditions for slip transmission:

1. The misalignment between the traces on the grain boundary plane made by the incoming and the outgoing slip planes should be minimized.
2. The magnitude of the Burgers vector of the residual dislocations left at the grain boundary after slip transmission has occurred should be small.
3. The outgoing slip system should have the maximum resolved shear stress (RSS) from the dislocation pile-up stress field.

They devised what is known today as the LRB criterion (Lee et al, 1989, 1990). This transmission indicator did not, however, explicitly incorporate the third condition, the RSS on the outgoing slip system. Candidate outgoing systems were instead represented by the Schmid factor and considered as a separate condition. An *in situ* EBSD on a duplex titanium alloy subjected to tensile tests investigated by Bridier et al. (2005) suggested that the Schmid factor may serve as a relevant parameter to predict the transmitted slip system on the condition that it can be activated. In the study on CP-Ti conducted by Wang et al. (2010), it was found that among the six available $\{10\bar{1}2\}\langle\bar{1}011>$ tensile twinning variants, the observed slip-stimulated twin lamellae had the highest m' value, while the Schmid factor based on the global stress state was a less significant indicator of twin activity. In a similar study on slip-induced tensile twinning in a Mg–Y alloy, Zhou et al. (2020) identified that the classical m' cannot explain the transmission, and it is the microscopic deformation that controls slip-to-twin transmission occurrences. Examining experimental characterization of slip transmission in several alloys, including HCPs, Bieler et al. (2014) drew the conclusion that different materials appear to have different dependencies on geometrical features, like slip directions, slip planes, and angle of the intersection of slip plane trace on the grain boundary plane. Since then, several criteria that account for weighted sum of these three conditions have been proposed (Bieler et al., 2014).

Apart from geometric criteria, a number of computational techniques have been built to model strain localization via intense slip bands. Most of them involved a local strain softening mechanism to formulate heterogenous deformations. Bréchet et al. (1993) were among the first to propose that heterogeneous plastic deformation in the form of slip bands is due to a local softening mechanism caused by the destruction of short-range order. This softening-based model has since been used to simulate strain localization in shear banding, dislocation channeling, and persistent slip bands in cubic materials using a finite element (FE) framework (Patra and McDowell, 2013, 2016, 2013; Sauzay et al., 2010; Sluys and Estrin, 2000; Zhou et al., 2006). Zhang et al. (2010) developed a shear-enhanced crystal plasticity constitutive relationship that reduced the slip resistance to account for the slip softening due to

breakdown of the short-range order. Using this constitutive model within a 2D crystal plasticity FE framework, they have simulated strain localization in a duplex Ti alloy. Notably, their simulated slip band structure was in qualitative agreement with experiments. Marano et al. (2019) applied an exponential decay in slip resistance implemented within a crystal plasticity Fast Fourier Transform (FFT) solver to capture strain localization in 2D and 3D polycrystal simulations. Through a systematic analysis of strain localization modes, they were able to distinguish slip and kink bands and simulate the evolution in their volume fractions. These simulations were carried out for an isotropic material with hypothetical parameters.

The localized plasticity via slip bands in a given grain would cause stress concentrations in its neighboring grain. From these slip band models, not studied in much detail is the stress field generated ahead of these localized slip bands. They also mainly focused on BCC and FCC metals and, for HCPs, only the basal systems were considered. Further, the effects of parent and possibly nearest neighboring grain orientation on slip band development and the possibility of blunting or triggering another slip band in the neighboring grain were not addressed.

The present study aims to identify the effect of grain neighbor orientation on slip band development, as well as its potential transmission into the neighboring grain. To this end, we present Slip Band FFT (SB-FFT), an extension of the full field EVP-FFT technique, that simulates the evolution of a discrete crystallographic slip band within an HCP crystal. The slip band is treated as a planar heterogeneity with a softening rate constitutive law distinct from the rest of the grain. The SB-FFT simulations focus on calculations of the local stress and strain fields and activated slip modes both within the parent grain and ahead of the band in the neighboring grain. We validate the model predictions by comparisons with previously reported experimental observations on CP-Ti, Mg–Y, and Ti64 alloys. The rate at which plastic shear strain concentrates in the band is shown to be sensitive to the orientation of the nearest neighbor, with plastically harder orientations facilitating slip band shear accumulation. Depending on the lattice orientation of the neighbor, the local reaction to the impinging slip band can be classified as either concentrated, suggesting slip band transfer, or distributed, implying slip band blocking. Finally, the analysis reveals a correlation between the c-axis misorientation of two neighboring grains and the type of slip system to which a slip band is anticipated to trigger a second localization.

The paper is structured as follows. In Section 2, we present the computational framework for modeling a discrete slip band development within a crystal embedded in a polycrystal. The model setup and choice of geometric and material parameters are discussed. Section 3 includes calculations of the local stress and strain fields for different HCP materials and nearest neighbor grain orientations. Section 4 is devoted to applying the model to interpret some experimental observations reported in the literature. Section 5 analyzes the effect of material and grain neighbor orientation on the propensity for the slip band to cause localization in the neighboring grain. Finally, Section 6 summarizes the main findings from this study.

2. Modeling framework

2.1. Numerical framework: the EVP-FFT approach

Over the last few decades, numerous studies have used strain gradient crystal plasticity models to simulate strain localization in polycrystalline materials (Arsenlis and Parks, 2002; Busso et al., 2000; Dunne et al., 2007; Niordson and Kysar, 2014; Sweeney et al., 2013; Zhang et al., 2018). For instance, using rate dependent crystal plasticity with updated lattice rotations, Zhang et al. (2018) captured grain-level slip, strain, lattice rotation and geometrically necessary dislocation (GND) density distributions in Ti–6Al–4V deformed in tension. In this work, we extend a different crystal plasticity model to simulate the development of an intragranular slip band in a polycrystal. The model builds upon the infinitesimal-strain formulation of the elasto-viscoplastic (EVP) fast Fourier transform (FFT) method developed by Lebensohn et al. (2012) to simulate heterogeneous deformation in polycrystals. EVP-FFT computes the spatially resolved intragranular micromechanical fields and macroscopic mechanical behavior of polycrystalline materials. This methodology can treat any number of intragranular heterogeneities with a given morphology and volume fraction, and these heterogeneous domains can adopt any crystallographic orientation and constitutive response distinct from the rest of the grain. As its name suggests, the EVP-FFT approach employs an elastic-viscoplastic constitutive potential for the material. The material model is discretized into a regular 3D grid of points, each at the center of a voxel. The solution procedure involves iteratively adjusting a compatible strain field and an equilibrated stress field until its constitutive potential minimizes the average local work at every material point in the model. Fourier transforms are used to perform simple products in Fourier space instead of solving convolution integrals in real space.

Many prior computational studies have employed the EVP-FFT framework to investigate the deformation behavior of polycrystalline materials (Eisenlohr et al., 2013; Kumar et al, 2017, 2020, 2017; Lebensohn et al, 2008, 2011, 2008; Lebensohn and Rollett, 2020; Montagnat et al., 2014; Nagra et al., 2017; Upadhyay et al., 2016). In close relation to the work here, recently, EVP-FFT has been employed to treat discrete twin lamellae or cracks within crystals. In the case of a twin, a planar twin lamella is the heterogeneous domain, defined by a predetermined set of voxels that are crystallographically reoriented to the orientation of the twin variant and within which the characteristic twin shear of the twin variant is imposed (Kumar et al., 2016). The model was, for instance, used to study the effect of local stress fields on twin growth and transmission across grain boundaries in HCP materials (Kumar and Beyerlein, 2020). To investigate the influence of microstructure variability on short crack growth, Rovinelli et al. (2015) used the EVP-FFT approach to model an elliptic crack by assigning void properties, i.e., infinite compliance, to a set of voxels inside a grain within an FCC Ni-based superalloy.

In the present work, a slip band is considered a heterogeneity with a different constitutive law within the EVP-FFT model. Similar to a crack or twin lamella, an intense slip band formed within a grain is a planar heterogeneity that bears a higher amount of shear. Furthermore, like a twin lamella, slip bands develop on crystallographic planes and in a particular crystallographic direction.

However, unlike a twin lamella, the amount of reorientation and shear associated with a slip band is not limited to or precisely defined by the atomic structure. Further, in a slip band, the amount of shear evolves with strain (or time) depending on the deformation history and local microstructure.

We first briefly review the portion of the formulation of the EVP-FFT model concerned with the constitutive law. A full presentation of EVP-FFT can be found in the original work by Lebensohn et al. (2012) and the extension for discrete twins in (Kumar et al., 2016).

The stress in an elasto-viscoplastic material at point $\mathbf{x}$ is given by Hooke's law:

$$\boldsymbol{\sigma}(\mathbf{x}) = \mathbf{C}(\mathbf{x}) : \boldsymbol{\varepsilon}^{\mathrm{e}}(\mathbf{x}) = \mathbf{C}(\mathbf{x}) : (\boldsymbol{\varepsilon}(\mathbf{x}) - \boldsymbol{\varepsilon}^{\mathrm{p}}(\mathbf{x})) \tag{3}$$

where $\boldsymbol{\sigma}(\mathbf{x})$ is the Cauchy stress tensor, $\mathbf{C}(\mathbf{x})$ is the elastic stiffness tensor, and the strain tensors, $\boldsymbol{\varepsilon}(\mathbf{x})$, $\boldsymbol{\varepsilon}^{\mathrm{e}}(\mathbf{x})$, and $\boldsymbol{\varepsilon}^{\mathrm{p}}(\mathbf{x})$ are, respectively, the total, elastic and plastic strain tensors at material point $\mathbf{x}$. Applying an appropriate implicit time discretization scheme provides the following for the stress at $\mathbf{x}$ at time $t + \Delta t$,

$$\boldsymbol{\sigma}^{\mathrm{t}+\Delta\mathrm{t}}(\mathbf{x}) = \mathbf{C}(\mathbf{x}) : \boldsymbol{\varepsilon}^{\mathrm{e,t}+\Delta\mathrm{t}}(\mathbf{x}) = \mathbf{C}(\mathbf{x}) : (\boldsymbol{\varepsilon}^{\mathrm{t}+\Delta\mathrm{t}}(\mathbf{x}) - \boldsymbol{\varepsilon}^{\mathrm{p,t}}(\mathbf{x}) - \dot{\boldsymbol{\varepsilon}}^{\mathrm{p,t}+\Delta\mathrm{t}}(\mathbf{x},\ \boldsymbol{\sigma}^{\mathrm{t}+\Delta\mathrm{t}})\Delta t) \tag{4}$$

where $\dot{\boldsymbol{\varepsilon}}^{\mathrm{p}}(\mathbf{x})$ is the viscoplastic strain-rate tensor. A viscoplastic flow rule is used to relate $\dot{\boldsymbol{\varepsilon}}^{\mathrm{p}}(\mathbf{x})$ to the stress tensor and all active slip systems at the same point, i.e.,

$$\dot{\boldsymbol{\varepsilon}}^{\mathrm{p}}(\mathbf{x}) = \sum_{s=1}^{N_s} \mathbf{m}^{\mathrm{s}}(\mathbf{x})\dot{\gamma}^{s}(\mathbf{x}) = \dot{\gamma}_0 \sum_{s=1}^{N_s} \mathbf{m}^{\mathrm{s}}(\mathbf{x}) \left(\frac{|\mathbf{m}^{\mathrm{s}}(\mathbf{x}) : \boldsymbol{\sigma}(\mathbf{x})|}{\tau_c^{s}(\mathbf{x})} \right)^{n} \ \mathrm{sgn}(\mathbf{m}^{\mathrm{s}}(\mathbf{x}) : \boldsymbol{\sigma}(\mathbf{x})) \tag{5}$$

where N_s is the number of slip systems made available to the material, and $\mathbf{m}^{\mathrm{s}}(\mathbf{x}) = \frac{1}{2}(\mathbf{b}^{\mathrm{s}} \otimes \mathbf{n}^{\mathrm{s}})$ is the symmetric part of the Schmid tensor of slip system s. Here $\mathbf{b}^{\mathrm{s}}$ and $\mathbf{n}^{\mathrm{s}}$ represent the Burgers vector and plane normal of slip system s. The scalars $\dot{\gamma}^{s}(\mathbf{x})$, and $\tau_c^{s}(\mathbf{x})$ are the shear rate and the slip strength (SS), associated with slip system s at point $\mathbf{x}$, respectively. The $\dot{\gamma}_0$ is a reference strain rate, usually the applied nominal strain rate, and n is the stress exponent. In Eq. (5), the term $\mathrm{sgn}(\mathbf{m}^{\mathrm{s}}(\mathbf{x}) : \boldsymbol{\sigma}(\mathbf{x}))$ enforces the slip rate direction to align with the glide direction.

2.2. Discrete slip band model

The slip band is treated as a region in which the resistance to slip, τ_c^{s}, decays at a rate proportional to the rate of slip (Melander, 1978; Olfe and Neuhäuser, 1988). Although the origins of such localized softening have yet to be clarified, the conventional argument is that it emerges due to a rise in local temperature generated by concentrated slip on a single slip system or slip plane (Alden, 1976; Armstrong et al., 2002; Dai et al., 2004). A significant number of experimental studies have related intense slip bands, regardless of their origin, with a low or negative work hardening in the material (Bapna and Meshii, 1974; Byun et al., 2006; Lai et al., 2015; Mori and Meshii, 1969; Neeraj et al., 2000; Sharp, 1972; Ulmer and Altstetter, 1991; Xiao and Umakoshi, 2002, 2003, 2004). For instance, Xiao and Umakoshi (2004, 2003, 2002) observed cyclic softening in the Ti–Al single crystal deformed by single and/or double prismatic slip. Sharp (1972) correlated the cleared channels of slip bands with the defect removal mechanism or local relaxation in copper crystals. To reflect this phenomenon, several crystal plasticity modeling studies have treated slip bands as regions experiencing material softening, in which the slip resistance decays with strain (Barton et al., 2013; Brechet et al., 1996; Erinosho and Dunne, 2015; Estrin and Kubin, 1986; Forest, 1998; Hure et al., 2016; Marano et al., 2019; Marano and Gélébart, 2020; Patra and McDowell, 2012, 2016, 2012; Xiao et al., 2015; Zhang et al., 2010). Zhang et al. (2010), for instance, used an evolution law allowing increased plastic strain rates to soften slip resistance on the basal and prismatic planes within the primary α-phase of a Ti–6Al–4V alloy. Marano et al. (2019) captured strain localization by using an exponential decay of the critical resolved shear stress, with a 20% maximum softening, with the accumulated slip on each system.

In the present study, at each material point $\mathbf{x}$ located within the pre-determined slip band domain, the slip strength (τ_c^{s}) for slip system s decreases proportionally with the rate of plastic strain ($\dot{\gamma}^{s}$) on that system, according to the following (Zhang et al., 2010)

$$\tau_c^{s,t+\Delta t}(\mathbf{x}) = \tau_c^{s,t}(\mathbf{x}) + \dot{\tau}_c^{s}(\mathbf{x})\Delta t,\ \dot{\tau}_c^{s}(\mathbf{x}) = -D_0 \tau_c^{s}(\mathbf{x})|\dot{\gamma}^{s}(\mathbf{x})| \tag{6}$$

Consequently, all active slip systems will soften and the slip band may be the consequence of multi-slip. Accordingly, the τ_c^{s} decays but remains non-negative. To avoid numerical instabilities, a lower limit of $\tau_c^{s} = 0.1$ MPa is set for all slip systems. The coefficient D_0 in Eq. (6) is a material-dependent rate coefficient for softening that governs how quickly shear localization occurs as straining develops. Due to its relationship to slip, it will likely depend on the applied temperature and strain rate. Here, these test conditions are not varied, and for the interests of this work, its value is fixed for a given material in all calculations that follow.

For material points outside the band in the same grain, slip strength (τ_c^{s}) and orientation remain constant with no hardening or softening, i.e.,

$$\dot{\tau}_c^{s}(\mathbf{x}) = 0,\ \tau_c^{s,t+\Delta t}(\mathbf{x}) = \tau_c^{s,t}(\mathbf{x}) = \tau_c^{s}(\mathbf{x})\big|_{\dot{\gamma}^{s}(\mathbf{x})=0} \tag{7}$$

This condition is made here for simplicity and is not a limitation of the model. Strain-hardening and lattice rotation could be considered in the model if desired, such as when large applied strains or a fully plastic response is being studied.

2.3. Embedded bi-crystal model setup

Fig. 1 shows bi-crystal model setup comprised of a parent grain, containing an explicit, discrete slip band, adjoined by its neighboring grain, without a slip band. The model uses periodic boundary conditions in all three directions. The model setup shown is the y-z plane of the periodic simulation cell. Within this plane, the parent and neighboring grains are similarly discretized into 100 × 200 voxels in the y and z directions, respectively. The simulation cell in the x-direction is three voxels thick. As shown, the bi-crystal is surrounded by a 20-voxel-thick homogeneous layer with uniformly distributed crystal orientations, intended to represent the average bulk response from the surrounding polycrystal. This value is determined to be sufficiently large such that the spatially resolved micromechanical fields are unaffected by the periodic nature of the imposed boundary conditions.

It is noted that regularly spaced grid required by the FFT formulation limits the spatial discretization and the description of grain boundaries or interfaces. That is to say, the current FFT approach lacks in capturing the interface-slip interaction induced by short-range spatial gradients in the micromechanical fields. This can be overcome by very fine discretization of the microstructure (i.e., high spatial resolutions), or using a non-local crystal plasticity formulation (e.g., strain-gradient theory) (Lebensohn and Needleman, 2016). However, both options significantly increase the computational cost. To circumvent the former issue, one can consider the most recently developed "composite voxel" technique (Marano and Gélébart, 2020). While capturing the slip band-grain boundary interaction is crucial for predicting highly localized fields at the intersection site, results reported here are not expected to be affected since they are concerned with longer range effects of neighboring grain lattice orientation on the slip band formation.

In the example setup shown in Fig. 1, for convenience, the slip band is made to lie at a 45° angle with respect to y-axis. Each crystal can take on any crystallographic orientation. The orientation of the parent grain is assigned such that the Burgers vector and slip plane normal of the slip band system lie in the y-z plane and respectively along the vectors **b** and **n** shown in Fig. 1. Accordingly, the parent grain orientation, when using Euler angles in Bunge convention, is $(90^\circ, 90^\circ, 45^\circ)$ when the slip band lies on a prismatic plane, and $(0^\circ, 45^\circ, 30^\circ)$ when it lies on a basal plane.

A preselected slip band with a given thickness w is embedded in the parent grain with its plane lying 45° with respect to y-axis, in which material can soften with application of a far-field strain based on the constitutive law described in Eq. (6). The crystallographic orientation of the parent crystal corresponding to a band, lying either on the basal plane or the prismatic plane, is shown using HCP crystal frames in Fig. 1. The orientation of the neighboring grain can vary. Uniaxial tension is applied along the y-direction, while the normal stress components in x- and z-directions are enforced to be, on average, zero. This state of stress would yield a Schmid factor of 0.5 for the slip system chosen for the slip band in the parent crystal.

2.4. Material properties

For most of this study, the SB-FFT calculations focus on slip bands in magnesium (Mg) and commercially pure titanium (CP–Ti). In Section 4, for validating the model with experimental studies, we additionally apply the model to an Mg–Y alloy and a Ti–6Al–4V alloy. Table 1 presents the properties of these four materials at room temperature, which includes the coefficient D_0 in Eq. (6), the anisotropic elastic constants, c/a ratio, potential slip systems, and their strengths (SS). For most of the studied materials, the order of magnitude of D_0 was determined so that the slip band would fully develop in the range of these materials within an applied strain of 1%. For the Ti–6Al–4V alloy, however, with high-resolution local strain measurements available, this coefficient was rigorously determined through a calibration process, as explained in Section 4.3. The stress exponent n in Eq. (5) is set to 10 for all of the simulations carried out here. A short study of the effect of the stress exponent on degree of localization is presented in Appendix A.

The elastic and plastic properties of Mg and CP-Ti are significantly different. As a measure of elastic anisotropy, we employ the universal measure of anisotropy A^L applicable to all crystalline materials defined by Kube (2016)[1], where the ideal case of elastic isotropy corresponds to A^L being zero. The anisotropy index of CP-Ti is $A^L = 0.075$, which is higher than the index of Mg, which is $A^L = 0.012$. Concerning plastic behavior, Mg is more plastically anisotropic than Ti, with ratio of SS values for the easiest to hardest slip mode of 1:11:26 (basal:prismatic:pyramidal) for Mg against roughly 1:2:3 (prismatic:basal:pyramidal) for Ti. For Mg, the easiest mode is basal with a very low SS, followed by prismatic, and finally pyramidal, which is the hardest. For Ti, however, the easiest mode is prismatic, followed by moderately harder basal, and then pyramidal as the hardest system.

2.5. Band thickness (w) effects

Cooperative, as opposed to independent, movement of dislocations on collective glide planes that are spatially correlated implies that several parallel glide planes with less than 10 nm spacing congregate to form a single slip band (Neuhäuser, 1983). A significant number of experimental studies have reported a finite thickness for observed slip bands, ranging from 0.1 μm to ∼ 2 μm (Bapna et al., 1968; Bapna and Meshii, 1974; Britton and Wilkinson, 2012; Lai et al., 2015; Weidner et al., 2006; Wejdemann and Pedersen, 2004; Xiao and Umakoshi, 2002, 2003). For instance (Bapna and Meshii, 1974), reported that the average thickness of slip bands in quench-hardened gold single crystals subjected to uniaxial tension is about 0.16 μm or equivalent to 850 consecutive {111} parallel

[1] The anisotropic index is defined as: $A^L = \sqrt{\left[\ln\left(\frac{\kappa^V}{\kappa^R}\right)\right]^2 + 5\left[\ln\left(\frac{\mu^V}{\mu^R}\right)\right]^2}$, where $9\kappa^V = C_{11} + C_{22} + C_{33} + 2C_{12} + 2C_{13} + 2C_{23}$, $15\mu^V = C_{11} + C_{22} + C_{33} - C_{12} - C_{13} - C_{23} + 3C_{44} + 3C_{55} + 3C_{66}$, $1/\kappa^R = S_{11} + S_{22} + S_{33} + 2S_{12} + 2S_{13} + 2S_{23}$, $15/\mu^R = 4\,(S_{11} + S_{22} + S_{33} - S_{12} - S_{13} - S_{23} + 3S_{44} + 3S_{55} + 3S_{66})$.

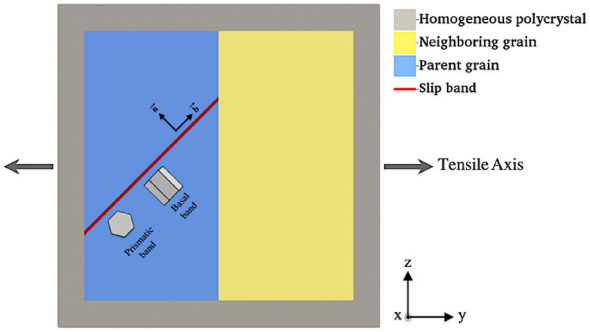

Fig. 1. Schematic of the bi-crystal unit cell under uniaxial tension in the y-direction. A two-voxel-thick ($w = 2$) slip band is shown in red embedded in parent grain. The hexagonal structures show the orientations of the parent HCP crystal corresponding to a prismatic or a basal slip band. The vectors **b** and **n** are, respectively, the Burgers vector and slip plane normal of the slip system on which the slip band localization occur. (For interpretation of the references to color in this figure legend, the reader is referred to the Web version of this article.)

Table 1
Softening coefficient D_0, elastic constants (Simmons and Wang, 1971), c/a ratio (Yoo, 1981), and slip strength (SS) values for different deformation modes for Mg (Beyerlein et al., 2011), CP-Ti (Wang et al., 2020), Mg–Y (Wang et al., 2021), and Ti–6Al–4V (Bridier et al., 2009). Note that only slip modes are employed to accommodate plastic deformation in the calculations.

Material	D_0	c/a ratio	Elastic constants (GPa)					Slip strength (SS) for deformation modes (MPa)			
			C_{11}	C_{12}	C_{13}	C_{33}	C_{44}	Basal $< a >$	Prismatic $< a >$	Pyramidal I $< c+a >$	Twin $\{10\bar{1}2\}$
Mg	10	1.624	59.8	23.2	21.7	61.7	16.4	3.3	35.7	86.2	20
CP-Ti	10	1.588	162.4	92.0	69.0	180.7	46.7	128	69	180	225 (Wang et al., 2017)
Mg–Y	30	1.624	59.8	23.2	21.7	61.7	16.4	22	85	90	13
Ti–6Al–4V	64	1.588	162.4	92.0	69.0	180.7	46.7	420	370	590	–

planes. From the atomic force microscopy (AFM) measurements of 83 slip bands within 12 grains in polycrystalline nickel, Weidner et al. (2006) found a wide spectrum of band thicknesses ($150 - 1150$ nm) and step heights ($2 - 25$ nm). While the slip band thickness varies in these studies depending on the material and loading conditions, a common observation is that slip band thicknesses are much smaller than the grain size. Therefore, for modelling slip bands, we need to choose a thickness that provides a localization effect, while remaining substantially thinner than its parent grain. Fig. 1 shows the slip band within a crystal, as represented by a planar domain of thickness w, described by two parallel boundaries, each of which represents the glide plane projected on y-z plane. Several simulations were conducted for a wide range of w from $w = 1$ to $w = 22$ voxels to identify an appropriate value. For the present calculations, we aim for a uniform region of slip along the band and across its thickness and to select the same thickness for all calculations hereinafter. A thickness of $w = 1$ is found unsuitable since the band develops discontinuously along its length, in stark contrast to experimental observations. For all bands with $w > 1$, localized slip eventually develops along the band. For $w > 2$, the fields within the band vary across the thickness of the band to a degree that depends on w. While the variation could have physical significance, this effect is not the phenomenon under investigation. In what follows, we use a slip band domain with $w = 2$, which produces uniform behavior across the width of the domain.

2.6. Cell thickness effects

The model microstructure is constant in the out-of-plane, x-direction, and therefore represents a columnar structure through thickness. To seek out any sensitivity in the results to the simulation cell thickness, calculations were repeated over a range of thicknesses from three to 100 voxels.

Fig. 2(a) shows the bi-crystal model cell that is 100 voxels thick, surrounded by a 20-voxel-thick buffer layer in y- and z-directions. The orientation of the parent grain is assigned such that the tilting plane on which the deformation is expected to be localized is a prismatic plane. The orientation of the neighboring grain is $(20^\circ, 151^\circ, 92^\circ)$. A tensile strain is applied along the y-axis.

Fig. 2(b) shows the contour of the projected resolved shear stress on the slip band system (SB-RSS) at the point when the y-axis uniaxial strain is 1%, when the unit cell is three voxels thick. As the strain is gradually applied along the y-axis, the stress and strain build in the buffer layer and two crystals and slip occurs. At some larger strain level, such as at the applied 1% shown, the slip band begins to develop more strain than its surrounding parent crystal. Around the band, the stress becomes heterogeneous, with localized stress field building in the neighboring crystal. Concomitantly, the stress reduces within and in the vicinity of the slip band. The same contours at the mid-plane of the bi-crystals with the 50 and 100 voxel thick unit cells are shown in Fig. 2(c and d), respectively. In all cases, the SB-RSS is lower in the band region, due to the localized softening, and heightened in the neighboring crystal. Comparing the

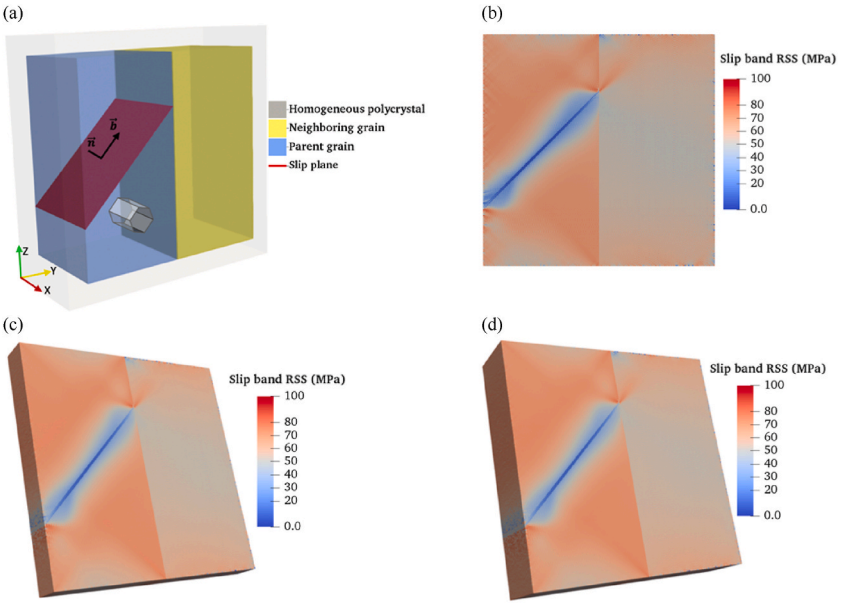

Fig. 2. (a) Schematic of a bi-crystal setup with a thickness of 100 voxels along the x-axis subjected to uniaxial tension in y-direction. The slip plane consists of two voxels through thickness ($w = 2$). Orientation of the parent crystal with a prismatic slip band is shown by an HCP crystal frame. Calculated distributions of the projected slip band resolved shear stress (SB-RSS) in CP-Ti for three different out-of-plane thicknesses along the x-axis: (b) three, (c) 50, and (d) 100 voxels. In (c, d), the stress contours are shown at the mid-planes of the cells. The surrounding homogeneous layer of polycrystal has been removed from the image in (b)–(d).

SB-RSS distributions among these three cell thicknesses finds their differences to be negligible. This consistency can be expected due to the fact that both Burgers vector and slip plane normal of the favored system with strain localization rest in the y-z plane and have no out-of-plane component. For computational efficiency, a cell thickness of three voxels is used for all calculations in this work.

3. Results

3.1. Grain neighbor-affected slip localization

We begin by studying the development of a prismatic slip band in CP-Ti under continued straining. The crystal is initially free of a slip band before application of the applied strain. In other words, while a domain for the slip band is preselected within the parent crystal, all material points in the parent crystal are strain-free before application of the far-field strain. The parent crystal has an orientation of $(90°, 90°, 45°)$ and the neighboring grain orientation is $(152°, 128°, 136°)$. As the far-field strain is applied, a slip band on a prismatic slip plane develops in the parent grain. At yield, the crystals begin to activate slip on one or more slip systems throughout the grain and in the slip band. Fig. 3 tracks the slip accumulated just on the prismatic slip system corresponding to the slip band, averaged over the parent grain ($\bar{\varepsilon}_M$) and also averaged solely across the slip band domain ($\bar{\varepsilon}_{SB}$) as the applied strain increases. At a

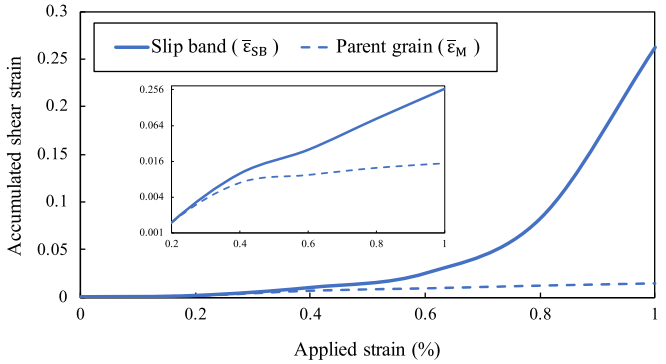

Fig. 3. Evolution of $\bar{\varepsilon}_{SB}$, the average accumulated plastic strain on the prismatic slip band system within the band domain, and of $\bar{\varepsilon}_M$ outside the band in the parent grain in CP-Ti. Inset: a semi-log plot for the strain range of 0.2–1% is shown in order to focus on the accumulated slip in the parent, as well as the separation in the evolution of accumulated slip within the slip band from that in parent, as the applied strain increases.

critical value of applied strain, 0.2% in this case, $\bar{\varepsilon}_M$ and $\bar{\varepsilon}_{SB}$ become non-zero, signifying that both the band and the matrix begin to slip. At a higher far-field strain, the slip band begins to accumulate more shear strain than its parent, as indicated by the $\bar{\varepsilon}_M$ and $\bar{\varepsilon}_{SB}$ curves splitting as the rate of accumulated slip within the slip band increases (see inset). At 0.56% macroscopic strain, the slip band accumulates two times more shear strain, on average, as its parent (i.e., $\bar{\varepsilon}_{SB} > 2\,\bar{\varepsilon}_M$). This situation, when a small fraction of the grain volume (here, ~1%) begins to sustain much more strain than its parent, represents the onset of localization. As the applied strain increases, the slip band shear $\bar{\varepsilon}_{SB}$ rapidly increases further, growing to be several times $\bar{\varepsilon}_M$.

Next, the simulation is repeated with the same parent and slip band but two other grain neighbor orientations. One grain neighbor orientation creates a higher misorientation (~89°) with the parent than the earlier example. Its orientation could also be considered a soft orientation, being more suitably oriented for prismatic slip with respect to the applied load. The second orientation has a similar misorientation (~64°) as the earlier example. But it is a relatively hard one, being even less suitably oriented for prismatic slip than the other two orientations. Here, we adopt an ad hoc conservative definition for "soft" and "hard" orientations, keeping in mind that there is in fact a spectrum of geometric hardness ranging from soft to hard. In particular, a soft and hard orientation respectively indicates a "low" or "high" geometric hardness for the easiest slip mode in that orientation. Quantitatively, it is measured by the maximum Schmid factor M_s among the slip systems of the easiest slip mode, which can range from 0 to 0.5. Between the two grain neighbors mentioned earlier, the soft neighbor has $M_s = 0.48$, while hard neighbor has $M_s = 0.09$. The properties of grain neighbor orientations for these three cases are listed in Table 2.

Fig. 4(a) compares the evolution of $\bar{\varepsilon}_M$ and $\bar{\varepsilon}_{SB}$ in the same slip band/parent grain for the three grain neighbor orientations. Regardless of grain neighbor orientation, the evolution of $\bar{\varepsilon}_M$ and $\bar{\varepsilon}_{SB}$ manifest in a similar manner. A finite amount of strain is required for slip to initiate in the parent and band, and with more strain, slip is seen to accumulate much faster in the band. If we, as before, consider as a measure of localization ε_{loc}, the macroscopic strain at which $\bar{\varepsilon}_{SB} > 2\,\bar{\varepsilon}_M$, we find that the nearest neighbor orientation affects how quickly the slip band accumulates shear strain. The higher misorientation neighbor, with the geometrically softer orientation has a localization strain ε_{loc} of 0.63%, while the neighbor with a similar misorientation as the earlier example, but with a harder orientation has a lower localization strain ε_{loc} of 0.51%. In another view, at the same applied strain of 0.63%, in the latter case the slip band would have nearly four times more shear strain than the parent, while in the former case, the slip band would have only two times more. At least in these three cases, the crystallographically harder neighboring grain promotes faster slip band localization. To demonstrate strain heterogeneity between the slip band and the parent grain, as well as between the two crystals, contours of equivalent plastic strain in these three cases are presented in Appendix B.

As more shear strain localizes in the slip band, the stresses locally in a zone ahead of the slip band are expected to rise concomitantly. In the present bi-crystal configuration, the slip band tip plastic zone lies in the neighboring grain at the slip band/GB junction. Fig. 5(a) plots the development of average von Mises stress in a small slip band tip volume of $6 \times 6 \times 3$ voxels (2-3 times in size than the band thickness) in the neighboring grain with applied strain. Alongside these curves, the evolution of the average von Mises stress for the entire neighboring grain is also plotted. In all cases, the stress in the slip band tip zone increases with applied strain, while the stress in the grain eventually softens in some cases. A stress concentration caused by the strain localization in the band can be identified by the amount the von Mises stress in the slip band tip zone at the slip band/GB junction exceeds the grain average. For CP-Ti, the stress concentration due to the slip band in all three neighbors increases as the applied strain increases beyond ε_{loc}, when the slip band has accumulated intense shear. The reason the moderate neighbor develops lower von Mises stresses than the soft neighbor, in this case, is the activation of secondary basal slip in the moderate one but not soft one. This difference likely contributed to its overall softness and reduced stress levels.

At the same time, the slip band and the parent grain in vicinity of the band develops a reaction stress, called a *back-stress*, that acts against slip. The back-stress is responsible for a decay in the total stress in the parent grain in the vicinity of the band as more strain is applied. Fig. 6(a) shows the evolution of the resolved shear stress on the slip band system (SB-RSS) within the vicinity of the band in the parent matrix, as well as in the entire parent grain, as the applied strain on a CP-Ti sample increases up to 1%. The RSS in the slip band vicinity is averaged over two parallel bands above and below the slip band domain, each with thickness of 2 voxels. Development of the back-stress is evident by the reduction in stress at the areas surrounding the band as the far-field strain rises beyond the localization strain ε_{loc}. These three cases indicate signs that the harder the neighbor is to deform, the more shear strain accumulates in the band, and

Table 2
Euler angles in Bunge convention, misorientation between the parent and nearest neighbor grain, and maximum Schmid factor among the systems of the easiest slip mode in CP-Ti and Mg bi-crystals.

Material	Easiest system	Neighboring grain orientation	Euler angles (degrees)			Maximum Schmid factor of the easiest system in the neighboring grain	Misorientation (degrees)
			φ_1	Φ	φ_2		
CP-Ti	Prismatic	Soft	353	174	254	0.48	89.3
		Moderate	152	128	136	0.24	68.3
		Hard	26	88	163	0.09	64.0
Mg	Basal	Soft	352	146	223	0.46	78.8
		Moderate	138	160	66	0.23	32.4
		Hard	93	81	259	0.05	85.8

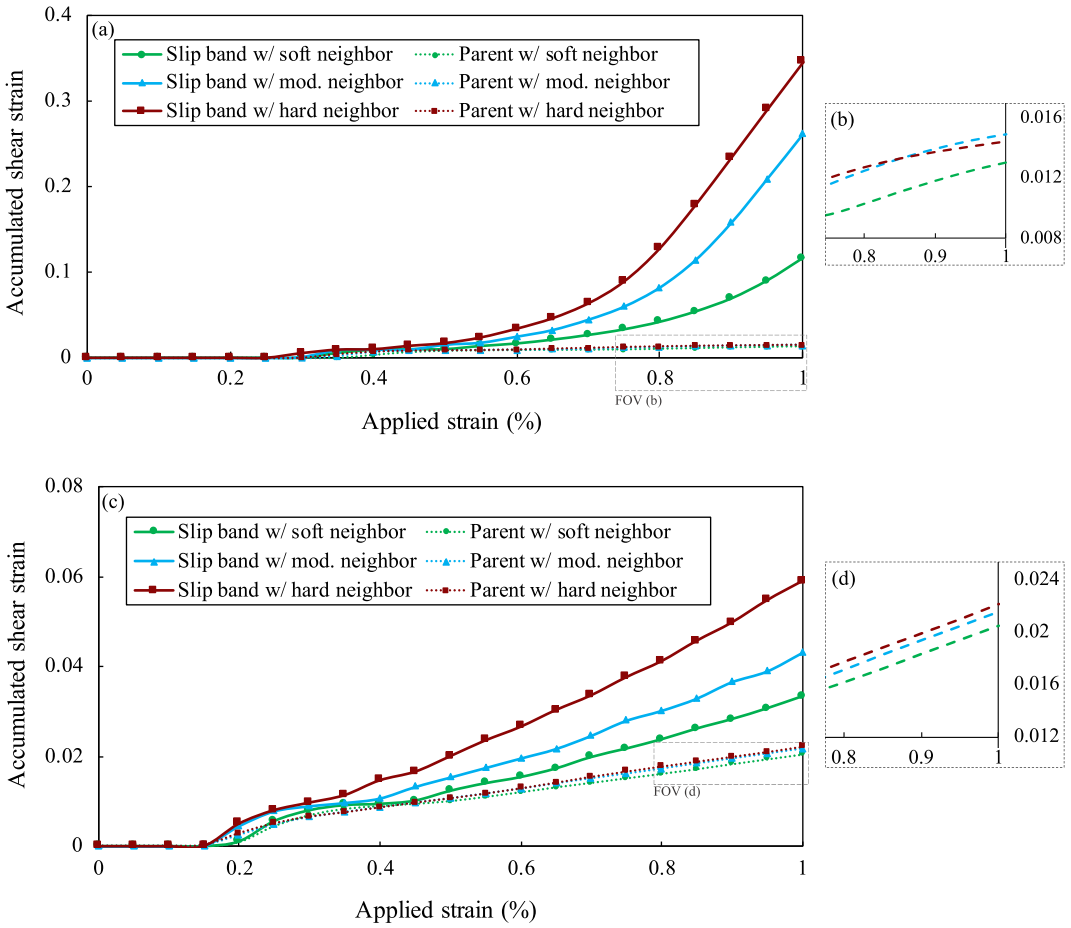

Fig. 4. Evolution of accumulated plastic strain on the slip band system within the band domain and in the parent matrix in three typical situations of soft, moderate, and hard neighboring grains for (a) CP-Ti and (c) Mg with a prismatic and a basal slip band, respectively. (b) and (d) are enlarged field of views selected in (a) and (c), respectively, and show the average plastic strain in the parent grains.

the higher back-stress is experienced by the parent grain around the slip band.

Next, we consider the same analysis but in another HCP metal, Mg. Compared to CP-Ti, Mg is a weaker material, wherein the SS values to activate slip in any of the slip systems in Mg are lower than those in CP-Ti (see Table 1). As another key difference, the preferred basal slip system in Mg is approximately ten times easier than the next easiest slip system, prismatic slip, whereas in CP-Ti the SS for prismatic slip is only half that of basal slip. In simulation, the Mg parent crystal orientation is $(0°, 45°, 30°)$. As in CP-Ti, for Mg, three different neighboring grain orientations are considered, representing either a geometrically hard, moderate, and soft orientation. These are defined by their suitability to activate basal slip with respect to the applied load. Their maximum Schmid factor among the basal slip systems respectively is $M_s = 0.05$, 0.23, and 0.46. Table 2 summarizes the geometrical parameters for these three cases.

Fig. 4(c) shows the evolution of the accumulated plastic strain on the slip band system within the slip band domain ($\bar{\varepsilon}_{SB}$) and in the parent grain ($\bar{\varepsilon}_{M}$) in Mg. Plasticity initiates earlier in all three cases in Mg compare to those in CP-Ti, a confirmation of the greater ease to activate basal slip in Mg than any of the slip systems in CP-Ti. The neighbor orientation has a similar effect on localization, with relatively harder neighbors causing the slip band to localize strain much faster than the softer neighbor. The noticeable difference, however, is that compared to CP-Ti, in Mg, the $\bar{\varepsilon}_{SB}$ is lower and the needed ε_{loc} for the onset of localization is larger. The associated development of and rise in von Mises stress in the zone ahead of the slip band tip in the neighboring grain are shown in Fig. 5(b). As seen in CP-Ti, the von Mises stresses generated by the slip band are the highest for the hardest neighbor. However, the stresses in the slip band tip zone do not necessarily lead to stress concentrations. In the hardest neighbor, the zone stresses are clearly above those of the average stress in the neighboring grain, signaling the development of stress concentrations, but, in the softest neighbor, the average stress in the grain are higher than in the zone, signifying no stress concentration.

As an assessment of back-stress development in the parent grain, for Mg, Fig. 6(b) shows evolution of the SB-RSS in the vicinity of slip band domain and in the parent grain as the applied strain increases up to 1%. Minimal back-stress development, or none in some cases, is observed. Comparing the amounts of reductions in Fig. 6(a) with (b) indicates that, regardless of grain neighbor orientation, CP-Ti is developing larger back-stresses than Mg. Higher back-stress development is a consequence of the larger strains that localize within the bands in CP-Ti, as seen in Fig. 4.

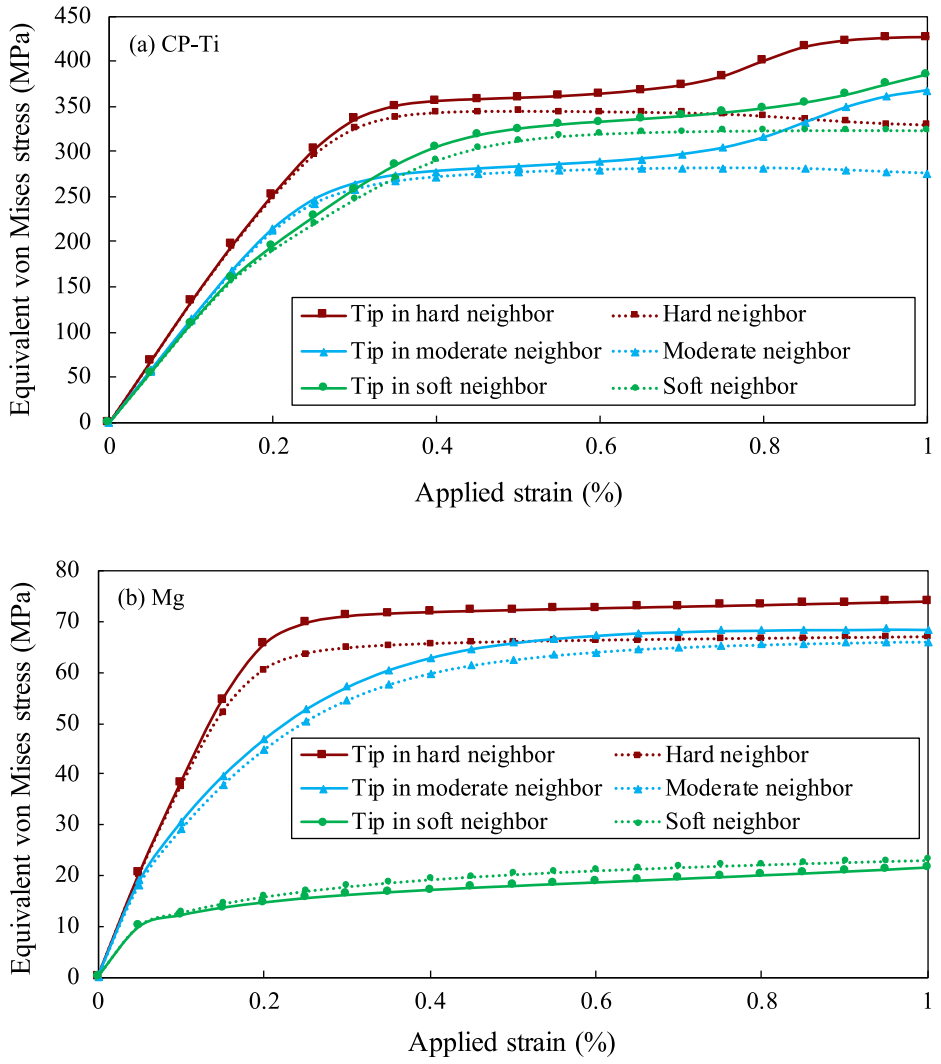

Fig. 5. Evolution of the equivalent von Mises stress in a small zone ahead of the slip band tip and in the interior of the neighboring grain for representative soft, moderate, and hard neighboring grains for (a) CP-Ti with a prismatic and (b) Mg with a basal slip band, respectively.

The few cases analyzed above suggest that the misorientation angle between two crystals has little effect on slip localization within the band, while the Schmid factor M_s of the easiest system in the neighboring grain has a much greater effect. To determine whether this effect is prevalent, the calculations are broadened to include several grain neighbor orientations, spanning the full range of possible grain boundary misorientations and levels of plastic hardness for CP-Ti and Mg. Fig. 7 presents the accumulated slip band strain $\bar{\varepsilon}_{SB}$ at uniaxial strain of 1% and the macroscopic strain ε_{loc} needed for the onset of localization for 33 distinct grain neighbor orientations. Here, $\bar{\varepsilon}_{SB}$ is normalized by $\bar{\varepsilon}_{M}$ in the parent grain, and the neighboring grain hardness is classified by the maximum Schmid factor of its easiest slip mode (prismatic slip for CP-Ti and basal slip for Mg). Fig. 7(a) reveals a correlation between the accumulated shear strain in the slip band and the hardness of the neighboring grain orientation for both metals. The plastically harder the neighboring grain (lower M_s), the faster the shear strain within the slip band intensifies. Fig. 7(b) shows that, concomitantly, the macroscopic localization strain ε_{loc} decreases for the harder grain neighbor. For some grain neighbor orientations in Mg, in both low and high Schmid factor domains, the onset of localization did not occur within the 1% applied strain and, therefore, they are not included in Fig. 7(b). Excluded orientations are provided in Appendix C.

Comparing the two materials, the weaker material, Mg, generally accumulates less strain in its slip band than the stronger material, CP-Ti, and requires more strain ε_{loc} for the onset of localization. As mentioned above, Mg, unlike CP-Ti, had a good fraction of neighbor orientations for which the localization strain ε_{loc} is not within the 1% applied strain. It is also found that the stronger elastic anisotropy in CP-Ti, compared to that in Mg, contributes to the accumulation of more strain in the band in CP-Ti (further details on the effect of elastic anisotropy on localization in slip bands can be found in Appendix D). Finally, the accumulated shear strain in the prismatic slip bands in CP-Ti exhibits a greater sensitivity to neighbor orientation than that in the basal slip bands in Mg.

Through the foregoing calculations and analysis, we have, thus far, identified a *neighbor-affected slip band localization* phenomenon.

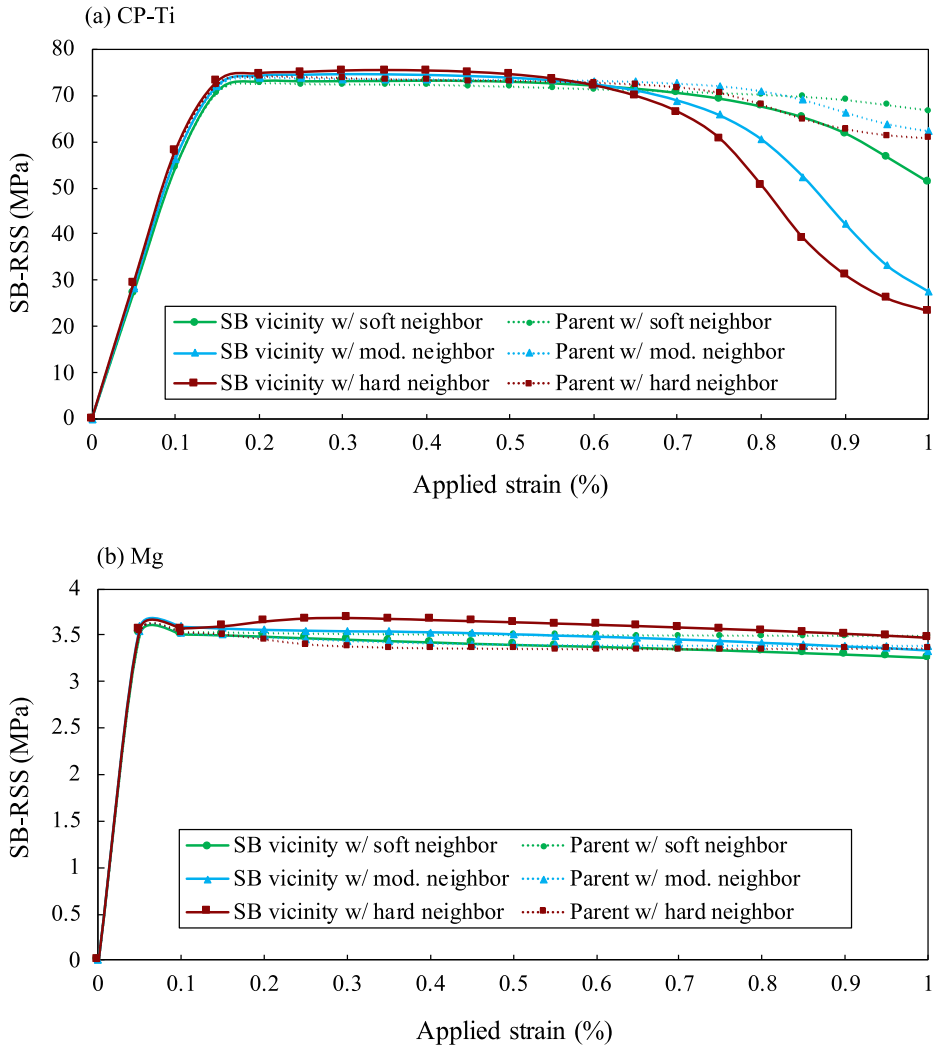

Fig. 6. Evolution of the resolved shear stress on the slip band system (SB-RSS) in the vicinity of the slip band domain and parent matrix in three typical situations of soft, moderate, and hard neighboring grains for (a) CP-Ti and (b) Mg with a prismatic and a basal slip band, respectively.

Regardless of material and slip band crystallography, a hard neighbor accelerates the development of the band localization in the parent grain and intensifies slip localization within it. In these cases, as the slip band intensifies, it will affect the deformation of the neighboring grain in a small zone ahead of the slip band. It should be noted, however, that these calculations assume slip band localization process is permitted to proceed continuously without disruption by another dissipation mechanism, such as void formation, grain boundary sliding, fracture, twinning, and formation of another slip band, particularly before the ε_{loc} is reached.

The calculation assumed, for simplicity, that no strain-hardening is induced by local slip associated with the slip band. Although this assumption could be lifted, it is worth noting that it is reasonable. Unlike cubic single crystals that exhibit four to five stages of work hardening, HCP crystals can exhibit a widely extended (50%–250% in Mg) initial stage of low strain hardening region (Hirsch and Lally, 1965). It results from an incapability of secondary slip caused by a deficiency of available slip systems. In agreement, in our simulations, we found the extent of secondary slip within the band domain is negligible (see Appendix E for more details), and thus, the strain-hardening associated by secondary slip may be excluded. Furthermore, since the grain neighbor orientation effect depends on the relative orientation of the easy (low SS) and hard (high SS) slip systems with respect to the applied loading, and as the strain-hardening will not change the slip strength ratio between the easy and hard slip systems, it is not expected that the present findings will change substantially upon incorporation of strain-hardening.

3.2. Identifying the active slip in the slip band tip zone and transmitted slip system

As seen in Fig. 5, for some grain neighbor orientations, the slip band can generate a concentration in stress in the neighboring grain. In these calculations, this stress is generally accommodated by a combination of elasticity and visco-plasticity by a number of slip

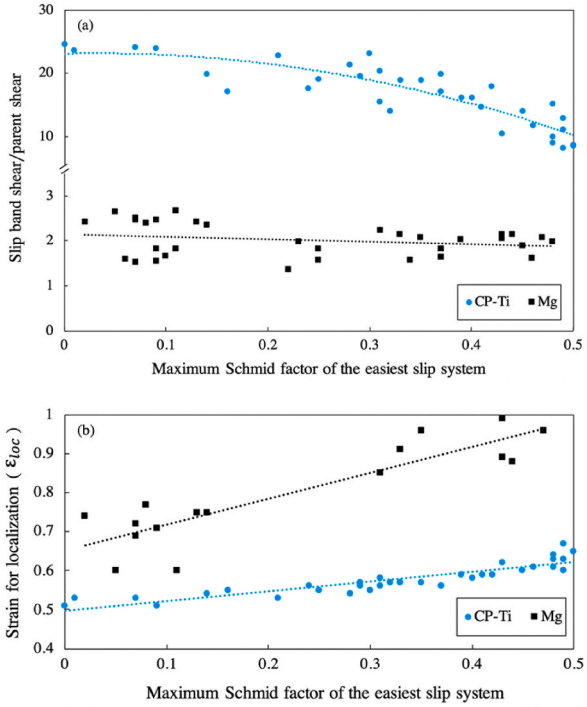

Fig. 7. (a) Average accumulated plastic strain on the slip band system within the slip band normalized by that in the parent grain for both CP-Ti and Mg at 1% macroscopic applied strain for a broad range of grain neighbor orientations, (b) Variations of the localization strain (ε_{loc}) with grain neighbor orientation for both CP-Ti and Mg. It is apparent that ε_{loc} for Mg bi-crystals are relatively higher than Ti, which can imply that slip bands develop earlier in Ti than they do in Mg. Note that some grain neighbor orientations in Mg for which the onset of localization did not occur within the 1% applied strain range are excluded in part (b).

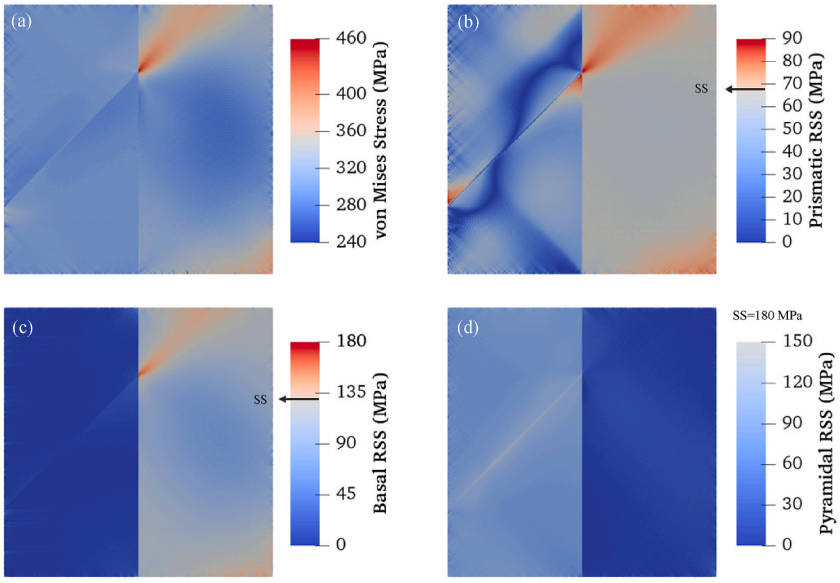

Fig. 8. In CP-Ti, (a) distribution of the von Mises stress in the parent grain containing a prismatic slip band and in its neighbor. The crystals are under one percent uniaxial strain. Development of a forward-stress is apparent, (b) Contour of the resolved shear stress (RSS) on a prismatic slip band system, (c) Distribution of the RSS on a basal slip system. The intense forward-stress at the tip implies the propensity of the basal activity in the neighboring grain despite the fact that it is not favorably oriented with respect to the applied load for basal slip, (d) The RSS distribution on a pyramidal plane shows no intensifying effect from slip band development. Note that the homogeneous surrounding layer has been removed from all images.

systems, which can easily belong to different modes. The calculated slip activity is that which is energetically favorable for accommodating the shear contributed by the slip band and applied load. In this section, for a few neighbor orientations, we probe the state of stress in a zone ahead of a slip band and the slip system(s) it could activate.

Fig. 8(a) presents the equivalent von Mises stress distribution at 1% macroscopic strain in a CP-Ti bi-crystal comprised of a neighboring grain with orientation of $(130^\circ, 147^\circ, 93^\circ)$, adjacent to a parent grain with a prismatic band. A zone of stress concentration is observed to develop where the slip band is terminated by the grain boundary. The interior of the neighboring grain distant from its boundaries experiences a lower state of stress.

To identify the slip systems that could be activated with further straining, the stresses are projected onto various candidate slip systems. Fig. 8(b)–(d) show the contours of the projected RSS onto a slip system from each slip mode: prismatic, basal, and pyramidal. The slip system shown developed the highest RSS in its mode. Each contour map is colored such that blue shades represent values below the slip strength (SS) and red shades above. The neighboring grain in this particular case is favorably oriented with respect to the applied load for prismatic slip. From the prismatic RSS map in Fig. 8(b), prismatic slip is already active in this grain, as indicated by the RSS equaling the SS for most of the grain. This is also confirmed by the accumulated slip contours found in Appendix F. At the slip band/GB junction, the projected RSS exceeds the SS, signifying a favorability to continue slip in this slip system at this site. The RSS map for basal slip in Fig. 8(c) suggests that basal slip could be triggered at the slip band/GB junction where the RSS exceeds the SS. Basal slip is, however, not active elsewhere in the grain, and, therefore, any basal activity would be localized and solely a consequence of the slip band. This outcome is also consistent with the accumulated slip contours (see Appendix F). Finally, as shown in the RSS map for pyramidal slip in Fig. 8(d), pyramidal slip is not active in the neighboring grain or near the slip band/GB site. For this nearest neighbor orientation, the slip band is likely not to transfer new slip onto a pyramidal slip system.

Any stress concentrations that develop in the neighboring grain where the slip band meets the boundary can potentially result in the "transmission" of slip across the GB via the formation of another slip band in the neighboring grain at the slip band/GB intersection. Should this occur, the new slip band would select a certain slip plane in the neighboring grain on which to form, one that is presumably energetically favorable and leads to maximum rate of energy dissipation. As mentioned in the introduction, the viability of transmission and likely transmission system have conventionally been identified based on maximum geometric alignment of the incoming and outgoing slip systems, such as m' in Eq. (2) (Luster and Morris, 1995). It has further been proposed that the question of transmission ought to additionally consider the RSS or Schmid factor M_s of the outgoing slip system with respect to the applied loading state (Lee et al, 1989, 1990). For the bi-crystal orientations considered in Fig. 8, the prismatic-prismatic transmission has the highest M_s (0.36) but low m' (0.03), whereas the prismatic-basal transmission has the highest m' (0.62) but a low M_s (0.17). The forecasted activity in the slip band tip zone in Fig. 8(b)–(c), however, suggests that either a prismatic-prismatic or prismatic-basal transmission are likely.

In Fig. 9, we examine, for a few more neighbor orientations, the slip system(s) that the slip band could activate in the neighboring grain based on the stress concentration developed at the band tip, and how they compare to expectations based on m' in Eq. (2), Schmid factor M_s, and the N parameter in Eq. (1). Table 3 summarizes the neighboring orientations, selected slip systems, and associated

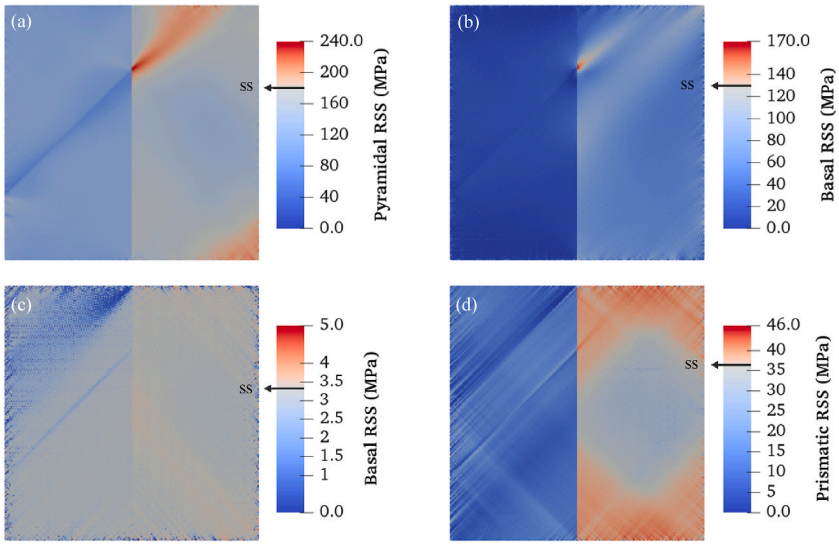

Fig. 9. Distribution of the resolved shear stress (RSS) on certain systems for different grain neighbor orientations (a–b) CP-Ti with a prismatic slip band and (c–d) Mg with a basal slip band: (a) Stress concentration developed ahead of the slip band is consistent with the incoming prismatic slip system and outgoing pyramidal slip system being well-aligned as suggested by high m', (b) An intense forward-stress on the basal slip system is developed despite of the low values of geometric factors for this prismatic slip to basal slip transmission, (c) There is no considerable forward-stress at the slip band tip zone, while the outgoing basal slip system is perfectly aligned with the slip band system, (d) A forward-stress is developed in the slip band tip zone despite the $m' = 0$ for the basal slip to prismatic slip transmission. Note that the homogeneous surrounding layer has been removed from all images.

Table 3
Neighboring grain orientation, c-axis misorientation between the two crystals, and geometric factors associated with slip systems shown in Fig. 9 for HCP bi-crystals.

Material	Band type	Part	Neighboring grain Euler angles ($\varphi_1, \Phi, \varphi_2$)	c-axis misorientation (degrees)	Selected slip system	Schmid factor	m'	N
CP-Ti	Prismatic	(a)	(22, 92, 307)	68.0	Pyramidal $(\bar{1}101)$ $[1\bar{2}13]$	0.43	0.93	0.88
		(b)	(263, 95, 259)	8.6	Basal (0001) $[11\bar{2}0]$	0.09	0.15	0.15
Mg	Basal	(c)	(207, 137, 112)	18.8	Basal (0001) $[\bar{2}110]$	0.48	0.89	0.87
		(d)	(266, 85, 198)	89.3	Prismatic $(10\bar{1}0)$ $[\bar{1}2\bar{1}0]$	0.49	0	0.99

Schmid factor M_s, m', and N for two CP-Ti (Fig. 9(a)–(b)) and two Mg (Fig. 9(c)-(d)) examples. It should be noted that the selected slip systems shown in Fig. 9 are not necessarily those with the highest RSS. Instead, they are selected to best elucidate the consistency between model predictions and geometric factors. Fig. 9(a) shows the pyramidal RSS map in a grain neighbor, which has a high c-axis misorientation with the parent grain, after uniaxial deformation of 1% strain. In this case the outgoing slip system studied has a high M_s, m' and N. Consistent with these geometric factors, the slip band tip zone generates a zone of high RSS that is intense and aligned with this system. Therefore, both the geometric factors and local stress fields suggest prismatic-pyramidal slip transmission in CP-Ti. For a different neighbor orientation, Fig. 9(b) presents the basal RSS map, also after 1% strain, wherein M_s, m', and N are all low for the selected basal system in neighboring grain. In contrast to these factors being low, the stress concentration ahead of the band on the selected basal plane is intense, suggesting that a prismatic to basal transmission is still likely in this case.

The basal RSS map in Fig. 9(c) considers a basal slip band in Mg with a neighboring grain orientation that, according to the high M_s, m', and N, is well suited for a basal-basal slip transmission based on ideal alignment. However, the RSS maps suggest that the slip band tip zone would not support this transmission, despite the nearly perfect alignment. Finally, Fig. 9(d) shows the prismatic RSS map to probe a potential basal-prismatic transmission in Mg. The stress concentrations suggest that such a transmission is supported by the local stress state, consistent with the high M_s and N, and in spite of the zero m'. Taken together, these four examples demonstrate that geometric alignment (N, m'), slip-band-tip stresses, and grain orientation (M_s) do not suggest the same outcome on slip transmission. Ultimately, comparisons with experiments would identify which indicator or indicators are useful. To this end, in the next section, we compare the SB-FFT model calculations with some observations reported in the literature.

4. Interpretation of experimental observations

Slip band transmission has been studied experimentally in a variety of HCP alloys and in a variety of ways. In this section, we apply the slip band model (SB-FFT) to some of these cases. In doing so, we consider other materials, apart from CP-Ti and Mg, and other microstructural configurations, mirroring the experimental ones. In particular, microstructural models advantageously deviate from the idealized planar geometry, wherein in place of the pair of grains sharing a common boundary that is planar, the curved morphology of the grain boundaries and orientation of slip band with respect to the load direction are taken into account in calculation. We, however, retain the homogeneous outer layer representing the bulk response from the surrounding polycrystal. Thus, effects of the sample free surface, sub-surface structure, and second-nearest grain neighbors, etc., are not captured. These effects could account for any second-order differences between the model predictions and experimental measurements. But, despite this, we find good overall agreement with experimental data.

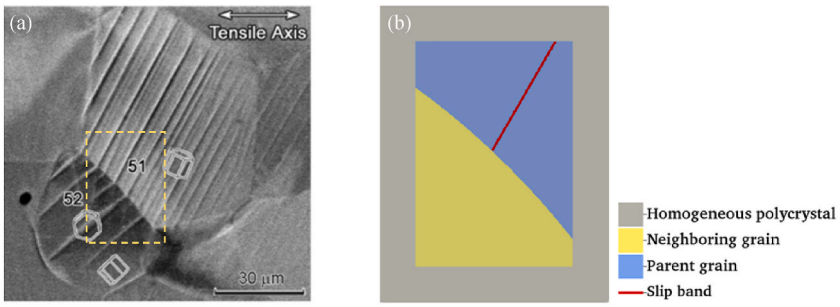

Fig. 10. (a) SEM image of the surface tensile areas in a CP-Ti sample deformed in bending shows that prismatic slip in one grain has caused $\{10\bar{1}2\}$ twinning in the neighboring grain through a slip-twin transmission process (Wang et al., 2010), (b) The bi-crystal unit cell with the preserved morphology of the grain boundary employed to validate the slip band model by simulating slip-twin transmission case shown in part (a). The image in (a) is taken with permission from (Wang et al., 2010).

4.1. Simulation of slip-stimulated twinning in CP-Ti

Wang et al. (2010) studied the slip to twin transmission across the grain boundaries in CP-Ti deformed in bending. Using the electron back-scattered diffraction (EBSD), they identified a few instances wherein prismatic slip bands and $\{10\bar{1}2\}\langle\bar{1}011>$ twin variants were connected across a grain boundary. Fig. 10(a) presents a SEM image from their work showing the development of $(1\bar{1}02)$ $[\bar{1}101]$ twin lamellae in a relatively small grain (grain #52), which is contiguous to a crystal with several parallel intense prismatic slip bands (grain #51). It appeared that the slip bands triggered the twins in the neighboring grain. The interesting questions are then why did prismatic bands not form and why did twins form instead, and with the particular V6 variant (see Table 4 for crystallographic information on different variants seen experimentally). Considering Schmid factors only would suggest that this neighboring grain is not well oriented for twinning since the variant with the highest Schmid factor, V6, has a low value of $M_s = 0.23$. A Schmid factor analysis would also suggest that it is not well oriented for prismatic slip since the highest value is $M_s = 0.26$. However, according to the m' factor in Eq. (2), it was better oriented for the observed prismatic-twin transmission (with $m' = 0.89$), than a hypothetical prismatic-prismatic transmission (maximum $m' = 0.47$).

Fig. 10(b) shows our model of these same two crystals surrounded by a homogeneous polycrystalline layer. The morphology of the prismatic band, grain boundary, and crystallographic orientations with respect to the load direction are preserved in the simulation setup. As in the experiment, the model microstructure is subjected to a far-field applied strain in the horizontal direction of the image, that starts at zero and is incremented quasi-statically to a maximum level of 2%, the level corresponding to the SEM image.

Fig. 11(a) shows the evolution with applied strain of the resolved shear stress (RSS) on a prismatic slip system and $(1\bar{1}02)$ $[\bar{1}101]$ twin system in the neighboring grain averaged over two regions: a finite-sized ($6 \times 6 \times 3$ voxel) region near the tip of the slip band, and the entire neighboring grain volume. The prismatic slip system shown is identified as the one with the highest calculated average RSS of all three prismatic slip systems in the tip region and likewise, the selected twin system, as the one with the highest calculated RSS among the six possible. The evolution of the RSS on the most favored prismatic slip system finds that the RSS increases with strain, but eventually the RSS is slightly higher on average in the grain than at the tip of the slip band. This implies that prismatic slip is favored less at the slip band tip region than elsewhere in the neighboring grain. In contrast, the results in Fig. 11(a) show that, unlike the average RSS in the grain, the twin RSS intensifies with strain at the tip of the slip band.

Fig. 11(b) shows the calculated distribution of the twin plane RSS for the $(1\bar{1}02)$ $[\bar{1}101]$ variant, the one seen experimentally and denoted as 'V6'. Consistent with the observation, we see that an intense stress concentration region develops ahead of the slip band for this twin variant. All other variants had a lower calculated RSS, and thus, the calculation would suggest that this variant would be the most favored among the six. To summarize, the calculations explain why a prismatic slip band did not form and the twin variant that is actually seen experimentally did. They further suggest that it would not have been selected without the slip band, as indicated by the calculations.

4.2. Simulation of slip-slip and slip-twinning transmissions in Mg–Y alloys

Recently, Zhou et al. (2020) used *in situ* SEM/EBSD on the Mg-5 wt% Y alloy to observe slip-slip and slip-twin transmission across a number of grain boundaries. Fig. 12(a) and (c) show a few micrographs from their work. For Fig. 12(a) at 5% uniaxial strain, they reported that basal slip band from G1 initiated a $(01\bar{1}2)$ $[0\bar{1}11]$ tensile twin in neighboring grain G2. In Fig. 12(c), at 2.5% strain, they found that the basal slip band in G3 resulted in another basal slip band and a $(1\bar{1}02)$ $[\bar{1}101]$ twin in G4. These two twin variants could be considered non-Schmid twins, since their Schmid factors were exceedingly low, just 0.005 (G2) and 0.23 (G4). The m' transmission factor was also low for some of these systems (see Table 4). Evidently, in these cases, the basal slip band led to twin formation, but the

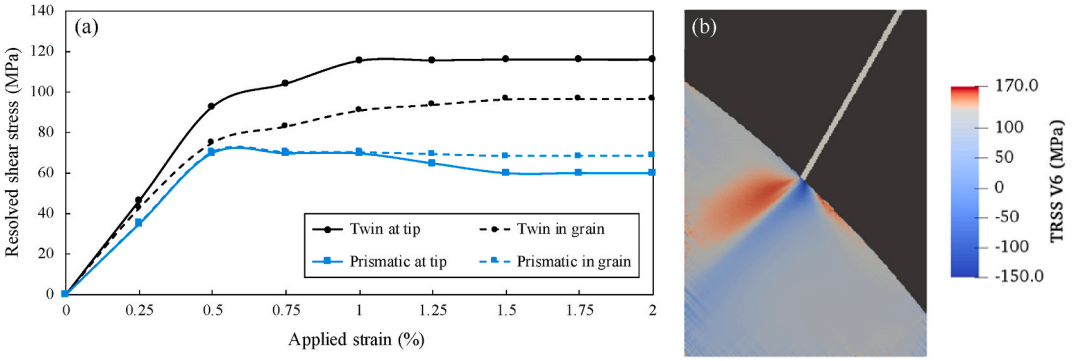

Fig. 11. (a) Evolution of the resolved shear stress on the prismatic and $\{10\bar{1}2\}$ twin planes as the macroscopic strain increases. The curves are shown for both the average RSS in the slip band tip zone only and in the entire neighboring grain, (b) Distribution of the twin plane resolved shear stress (TRSS) for the $(1\bar{1}02)$ $[\bar{1}101]$ tensile twin variant (V6) at 2% macroscopic strain. The surrounding homogeneous layer has been removed from the image.

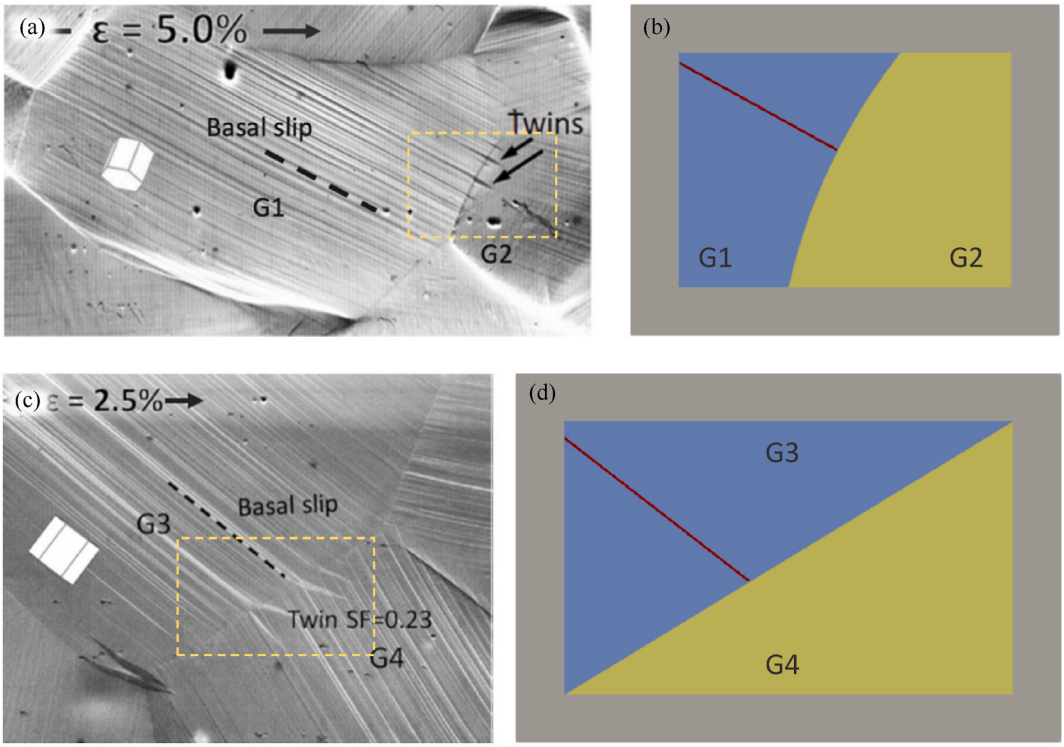

Fig. 12. SEM image of two pairs of grains at the surface of an Mg–Y sample subjected to uniaxial strain of (a) 5%, and (c) 2.5%. In each case, the basal slip in one grain is linked to $\{10\bar{1}2\}$ twins and/or another basal slip band in the neighboring grain (Zhou et al., 2020), (b, d) Bi-crystal setups with preserved morphology of the grain boundary used to model two slip transmission cases shown in parts (a) and (c). The images in (a) and (c) are taken with permission from (Zhou et al., 2020).

reason behind the variant selection is not clear.

To determine if slip band tip stresses could provide an explanation, models of bi-crystals embedded in a homogeneous medium are constructed, with the same crystal orientations and grain boundary orientation as the experiment, as shown in Fig. 12(b) for the G1/G2 pair and Fig. 12(d) for the G3/G4 pair. In each model, the parent grain contains a region for which a basal slip band belonging to the slip system identified in the experiment can evolve with strain. In simulations, the strains are applied in tension in the same orientation with respect to the microstructure up to a strain level of 5% (for G1/G2) and 2.5% (for G3/G4). Properties of the Mg–Y alloy used in the calculations are presented in Table 1. To identify the likely twin or slip system to be activated in the neighboring grains, we analyze in Table 4 the calculated RSS/SS ahead of the slip band for all six $\{10\bar{1}2\}$ twinning variants, as well as the basal, prismatic, and pyramidal <c+a> system with the highest RSS. Although twinning is not considered as a dissipative mechanism in our crystal plasticity calculations, as a reference, some previously characterized estimates for a critical resolved shear stress for tensile twinning on $\{10\bar{1}2\}$ planes are included in Table 1.

The calculated ratios acquired at 5% strain for the G1/G2 bi-crystal predict that among the six twin variants, the $(01\bar{1}2)\ [0\bar{1}11]$ twin variant (V2) has the highest resolved shear stress and, therefore, will be activated first. This is the same variant as seen experimentally. The RSS/SS ratio for all of the slip systems are lower than 1.0, indicating that the stress state generated by the slip band would not especially result in slip in the neighboring grain. Fig. 13(a) shows the evolution of the RSS/SS ratios for the basal, prismatic, and pyramidal system with the highest RSS at the slip band tip as well as the twin RSS for the twin variant V2 in grain G2, as the macroscopic strain increases. Over the straining period, not only are the RSS/SS ratios for all slip systems lower than 1.0, but they are less at the band tip than in the neighboring grain on average. Furthermore, the calculations imply that the slip band stress state selected this variant (V2) to be activated.

Likewise, in the bi-crystal modeled for G3/G4 pair, as presented in Table 4, calculations show that among all twin variants, the $(1\bar{1}02)\ [\bar{1}101]$ variant (V6) has the highest propensity for activation. The RSS/SS ratio for the basal slip is higher than 1.0, suggesting also the likelihood of activating basal slip in grain G4 at the grain boundary. Calculations of the evolution of the RSS/SS in Fig. 13(b) indicate that although the overall stress in the grain is sufficient to activate both the V6 twin variant and basal slip, the band intensifies the RSS values for these two deformation modes at the boundary. These variants are the same as those seen experimentally.

Table 4
Schmid factor, m', and ratios of RSS/SS averaged at the band tip and over the entire grain associated with $\{10\bar{1}2\}$ twin variants as well as basal, prismatic, and pyramidal slip systems in grains G2 and G4 shown in Fig. 12.

		Tensile twinning						Slip modes		
		V1	V2	V3	V4	V5	V6	Basal	Prismatic	Pyramidal
	Slip/twin plane normal	$(10\bar{1}2)$	$(01\bar{1}2)$	$(\bar{1}102)$	$(\bar{1}012)$	$(0\bar{1}12)$	$(1\bar{1}02)$	(0001)	$(10\bar{1}0)$	$\{10\bar{1}1\}$[a]
	Slip/twin direction	$[\bar{1}011]$	$[0\bar{1}11]$	$[1\bar{1}01]$	$[10\bar{1}1]$	$[01\bar{1}1]$	$[\bar{1}101]$	$[\bar{2}110]$	$[\bar{1}2\bar{1}0]$	$<\bar{2}113>$
G1 → G2	Schmid factor	− 0.21	0.005[b]	− 0.41	− 0.24	− 0.01	− 0.38	0.22	0.47	0.49
	m'	0.62	0.20[b]	− 0.35	− 0.17	0.002	0.24	0.74	0.14	0.07
	RSS/SS at tip	0.6	2.2[b]	1.0	0.6	2.2	1.3	0.93	0.92	0.90
	RSS/SS in grain	− 4.1	− 0.1[b]	− 5.7	− 4.3	− 0.1	− 5.5	0.96	0.98	0.92
G3 → G4	Schmid factor	0.24	0.33	0.17	0.19	0.33	0.23[b]	0.47	0.15	0.44
	m'	0.62	0.07	− 0.16	− 0.16	0.29	0.83[b]	0.85	0.10	0.001
	RSS/SS at tip	4.41	3.26	4.75	4.39	3.29	4.94[b]	1.24	0.27	0.55
	RSS/SS in grain	2.25	3.64	2.42	2.08	3.74	2.67[b]	1.07	0.21	0.52

[a] Presented data corresponds to $(1\bar{1}01)$ $[\bar{2}113]$ and $(\bar{1}101)$ $[1\bar{2}13]$ 1st order pyramidal <c+a> slip in G2 and G4, respectively.
[b] Operating twin variant.

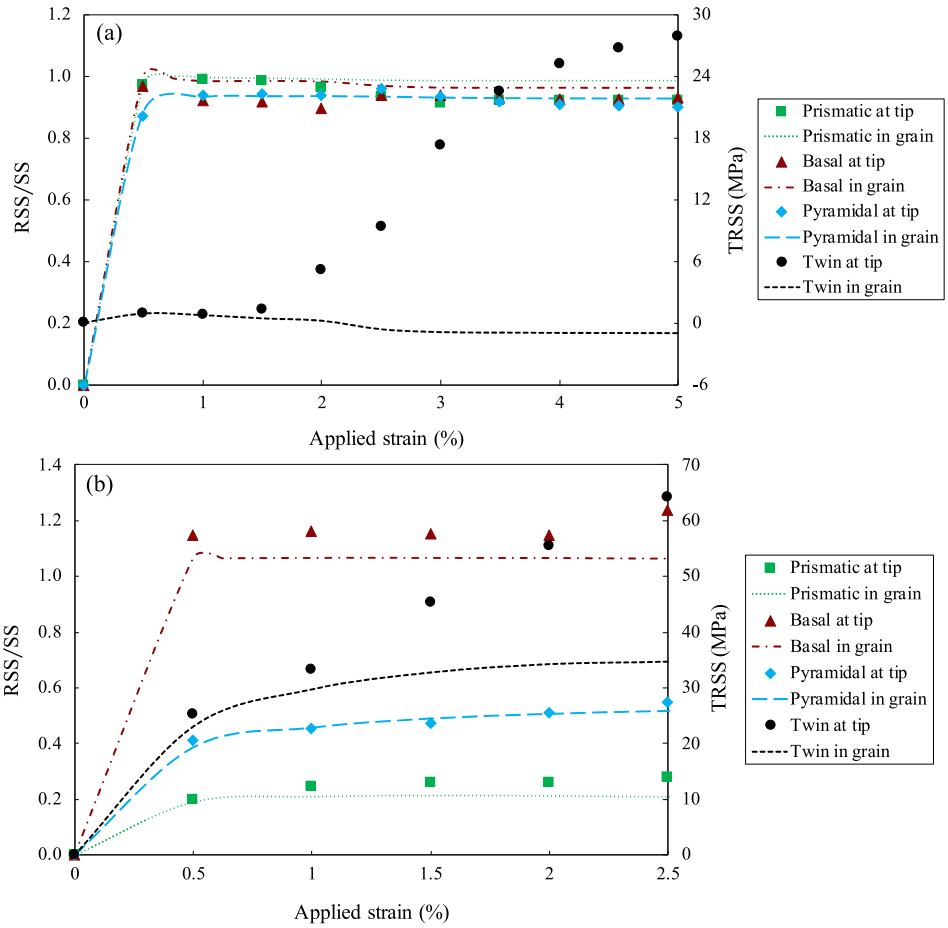

Fig. 13. Evolution of the ratio of the resolved shear stress (RSS) to slip strength (SS) for different slip modes and the twin plane resolved shear stress (TRSS) for the most favored $\{10\bar{1}2\}$ twin variant as the applied strain increases, for (a) G1→ G2 and (b) G3 → G4 transmission cases shown in Fig. 12. The datapoints represent the average RSS in the band tip domain while dashed curves show that in the entire neighboring grains G2 and G4.

4.3. Simulation of serial slip transmissions in microtextured Ti–6Al–4V titanium

Utilizing an *in situ* high resolution scanning electron microscope digital image correlation (SEM DIC) technique, Echlin et al. (2016) studied the long-range plastic strain localization in a microtextured Ti–6Al–4V sample. A microtextured region within the sample refers to a broad mm-scale band of grains that are closely oriented, typically with misorientations from 5° to 30°. They reported that not only could slip bands develop at strains lower than macroscopic yielding in the microtextured region, but they also successively transmitted from one slip mode in one grain to the same mode to its neighboring grain. Long chains of prismatic-to-prismatic, as well as basal-to-basal slip transmissions developed across the deformed sample. Such a chain of slip bands transmitting from one grain to another within regions where neighboring grains were closely oriented, was also observed in another Ti alloy in (Bridier et al., 2005).

The bi-crystal configuration shown in Fig. 1 is used to model the slip band development and the resulting stress concentration in Ti–6Al–4V tensile samples, for which the material properties are presented in Table 1. To represent a typical pair of grains in the microtextured region, the orientation of the parent grain is assigned, so that either prismatic or basal slip is favorable and that of the neighboring grain makes an angle of 30° or less with the c-axis of the parent. We find that for a softening coefficient D_0 of 64, the strain levels in the slip band and the parent grain for a range of neighboring orientations are, on average, comparable to the experimentally measured values. Fig. 14 shows one such case where the DIC measurement of the normal strain along the loading direction at 0.77% macroscopic strain are compared with the same component calculated in the parent matrix and slip band at the same macroscopic strain (the surrounding simulated material is removed from the image). The neighboring orientation in this case is $(262°, 104°, 86°)$.

Fig. 15(a) shows the measured normal strain along the loading direction made by Echlin et al. (2016) at 0.86% macroscopic strain level. The microstructure shown contains both strongly textured microtextured regions separated by regions of low texture. The slip bands seen in grains across the microstructure exhibit a range of intensities. As validation, slip band calculations are repeated for three different nearest neighbor grain orientations, that span the likely c-axis misorientations, 12°, 72°, and 89°, seen in Fig. 15(a). Fig. 15 (b–d) presents the calculated strain fields in the slip band at the same 0.86% macroscopic strain. By only changing the grain neighbor orientation, a similar range of band strains as seen experimentally is achieved.

To identify the role that the localized slip band tip stresses in the neighboring grain could play in transmission, calculations were carried out for a number of grain orientations spanning distinct c-axis misorientations from 0° to 30°. Fig. 15(e) maps the accumulated slip on the dominant system (i.e., the most stressed system) in the slip band tip zone versus the c-axis misorientation. In most cases, we find that only one or at most two slip systems are activated ahead of the band. The map shows that for any c-axis misorientation of less than 30°, a prismatic slip band is anticipated to transmit onto a prismatic slip system in the neighboring grain. Likewise, for the parent grains with a basal band, a high propensity of a basal-basal transmission is expected. However, when the misorientation approaches 30°, either several slip systems with nearly equal accumulated slip are activated, or in rare cases, a basal to non-basal slip transmission is indicated. The interpretation here is that either a basal or prismatic slip band could have triggered a same-slip transmission across grain boundaries with $<30°$ c-axis misorientations.

5. Assessing the propensity of slip transmission from a slip band

To date, criteria for slip transmission and the transmission pathways have been based solely on the relative orientations of the incoming and outgoing slip systems in question and Schmid factors based on the applied state of stress but not on properties of the material or local stress generated by the slip band. As we have shown here, in some cases, depending on the neighboring orientation, slip or twin activity that is distinct from that in the rest of the grain can occur. As a final study, we employ the model to identify situations in which slip transmission from a slip band into a neighboring grain is likely and the slip system(s) to which the transmission event occurs. Using the calculations, we link these conditions with the slip activity generated ahead of slip band in the neighboring grain.

The slip activity triggered in the neighboring grain at the tip of a slip band can either labeled as *concentrated* or *distributed*. Concentrated slip corresponds to only one or at most two activated systems. Any slip system with the projected RSS/SS ratio greater

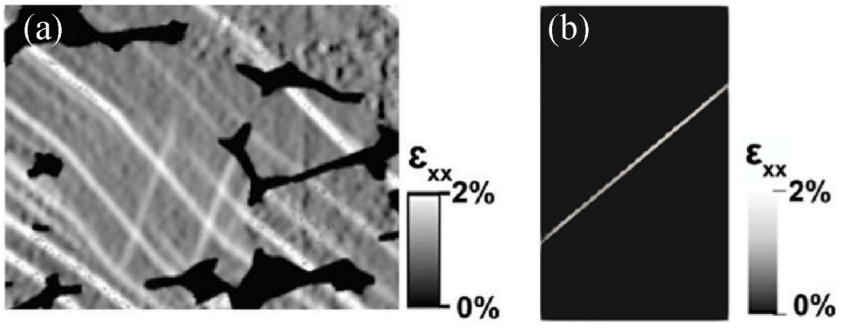

Fig. 14. DIC measurement (Echlin et al., 2016) (a), and calculated (b) distribution of the normal strain along the loading direction in the prismatic slip band and the parent matrix, at 0.77% macroscopic strain. The surrounding homogeneous layer and the neighboring crystal have been removed from the image in (b). The image in (a) is taken with permission from (Echlin et al., 2016).

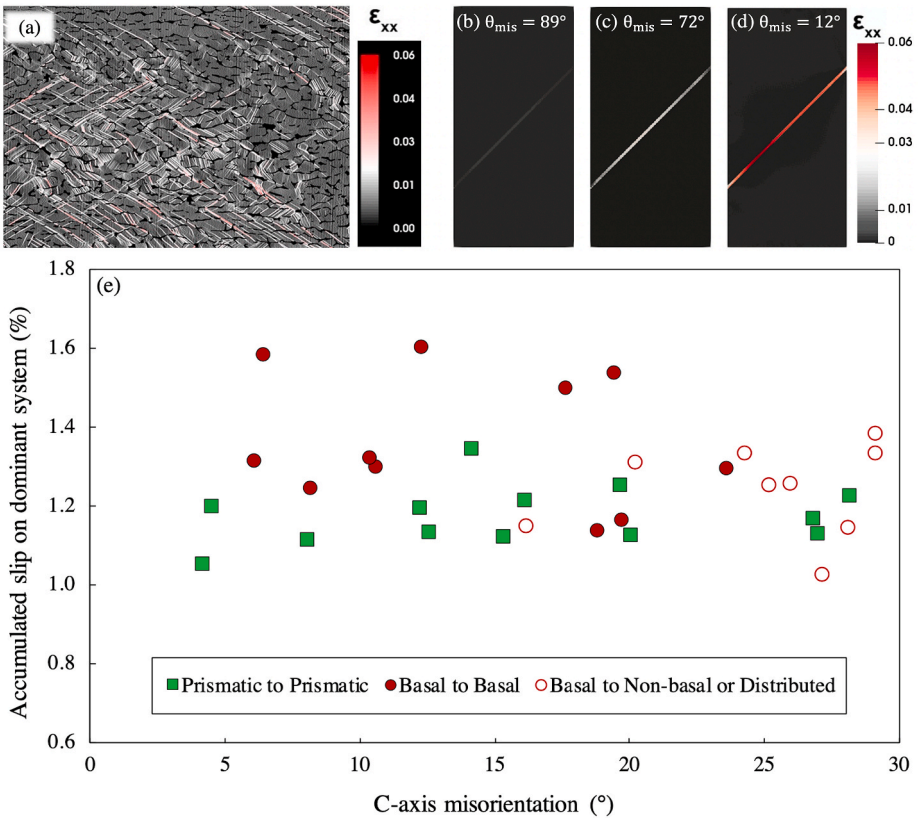

Fig. 15. (a) SEM DIC measurement of the normal strain along the loading direction for a Ti–6Al–V4 tensile sample at 0.86% macroscopic strain (Echlin et al., 2016), (b–d) Simulated distributions of the normal strain along the loading direction in the parent grain at 0.86% macroscopic strain from three representative parent/grain neighbor pairs show a same range of strain localization within the band compared to experimental data, (e) Accumulated slip on the dominant system in the slip band tip zone against the c-axis misorientation of two adjacent crystals. Both prismatic and basal slip bands are predicted to transmit onto a slip system of the same mode in the neighboring grain for low misorientations. In (b)–(d), the surrounding homogeneous layer and the neighboring crystal have been removed from the image. The image in (a) is taken with permission from (Echlin et al., 2016).

than one is considered as an *activated system* by slip band. The RSS/SS of the second activated system could be equal or close to the highest one, within 90% of the ratio for the first system. Concentrated slip is considered here as a signature of slip transmission and the activated slip system(s) the selected ones for transmission. Distributed slip, on the other hand, occurs when there are three or more activated systems and is usually associated with plasticity dispersed more or less equally on many slip planes.

Considering again a pair of CP-Ti crystals within a polycrystal, we investigate the effect of neighboring grain orientation on the likelihood of slip transmission from a prismatic slip band into a neighboring grain and the slip system(s) to which the transmission event occurs. A broad range of orientations, including 50 distinct neighbor orientations are considered in the calculations. Fig. 16 presents the c-axis misorientations that lead to one of three cases, concentrated slip on a slip system belonging to the same slip family as the slip band, concentrated slip on a system belong to a different family, or distributed slip. Similar to other geometric factors, such as m' and Schmid factor, no strong correlation between the c-axis misorientation and the propensity of slip transmission is detected. However, the type of slip system onto which incoming slip band is anticipated to transmit correlates with the misorientation angle. In particular, it is apparent from Fig. 16(a) that for a prismatic incoming band in CP-Ti, slip in parent grain transmits to a prismatic system in the neighbor grain when the misorientation is small. For high misorientations on the other end, transmission to a different family of slip systems, such as basal or pyramidal, is expected. Lastly, for the moderate misorientation angles, likely systems for transmission are combined of a prismatic and a basal plane.

Basal slip bands may also develop in certain grains of CP-Ti and, in Fig. 16(b), we present the slip transmission map from a similar set of calculations for a basal slip band. Since the slip resistance on prismatic planes in CP-Ti is the lowest among all deformation modes, basal to prismatic transmissions are evident in a broad range of misorientations. Moreover, due to the fact that pyramidal <c+a> slip has the highest strength (SS), among all bars representing 'basal or pyramidal' in Fig. 16(a) and 'prismatic or pyramidal' in Fig. 16(b), only a few correspond to the pyramidal slip.

Fig. 17(a) and (b) maps the concentrated vs distributed slip activity against the c-axis misorientation between two adjacent grains for basal and prismatic slip bands in Mg, respectively. The same trends as what explained for CP-Ti are realized for Mg, except for a few distinctions. Firstly, since pure Mg has a high plastic anisotropy, i.e., the difference between SS values of different slip modes is

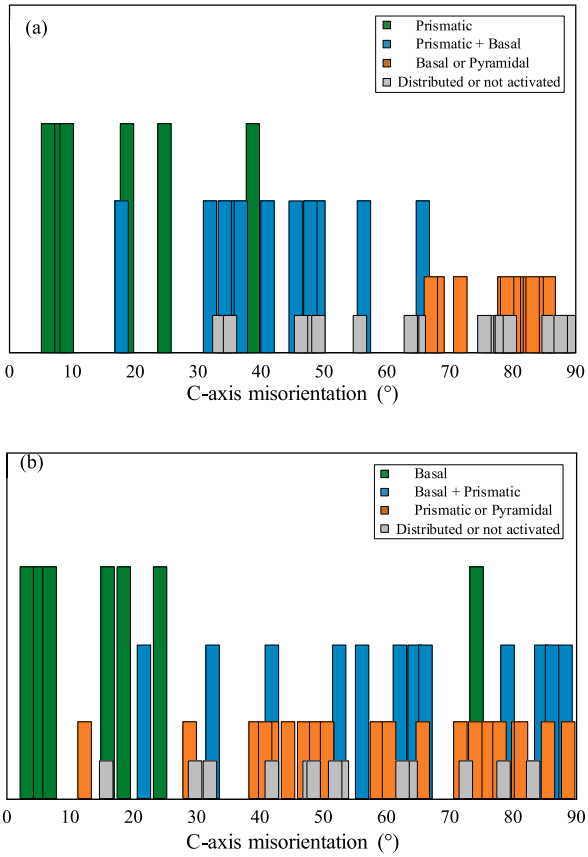

Fig. 16. Slip activity generated ahead of the slip band in the neighboring grain against the c-axis misorientation between two adjacent crystals for (a) prismatic, and (b) basal band type in CP-Ti. Presented data suggests that when the misorientation is small, transmission to a like system is expected, while for high misorientations, slip in the parent grain is predicted to transmit onto an unlike system in the grain neighbor. Note that most of the orange bars represent either a basal or a prismatic slip and only a few correspond to the pyramidal slip. The height of the bars has no physical meaning; the height differences are only used to distinguish the cases from one another. (For interpretation of the references to color in this figure legend, the reader is referred to the Web version of this article.)

significantly large, pyramidal slip – the hardest slip mode – is not activated in any misorientation angle. Moreover, numerous instances of the easy basal slip are identified as basal to basal transmissions shown ubiquitously in any misorientation angle in Fig. 17(a) and as prismatic to basal transmissions shown in moderate-high misorientations in Fig. 17(b).

Considering the maps for different band types and materials presented in Figs. 16 and 17, exclusive transmission to the same slip family as the incoming band at small misorientation angles is prevalent. This implication was also presented earlier for Ti–6Al–4V titanium alloy in Section 4.3., where the model was validated against an experimental study reported in (Echlin et al., 2016). In addition to that, occurrences of prismatic to prismatic slip transmission at low misorientation angles are recognized by Kehagias et al. (1995), who investigated the slip transfer mechanisms across low-angle grain boundaries in a deformed titanium sample.

We have shown that the slip band tip stress-based criterion proposed in this work can be utilized for identifying the nearest neighbor orientations in which slip band transmission is possible and the likely slip system for which it occurs. Additionally, there are other areas where the slip band model and the stress-based criterion can be useful. For instance, in a post-mortem analysis of a slip transmission across the grain boundary, it might not be easy to recognize the grain in which slip bands have formed first and then initiated the slip (or twin) in the neighboring grain. By studying the local stress fields and possible stress concentrations at the band tip, the sequence of events can be identified. The local stress fields at the band tip predicted by SB-FFT model can also be measured experimentally. Using the high-resolution electron backscatter diffraction (HR-EBSD) technique, Britton and Wilkinson (2012) and Guo et al. (2014) measured the resolved shear stresses on specific slip systems ahead of the slip bands in CP-Ti. In a different series of studies (W. Abuzaid et al., 2012a; W. Z. Abuzaid et al., 2012b; Tatschl and Kolednik, 2003), using high resolution *ex-situ* digital image correlation (DIC) and EBSD techniques, researchers measured plastic strain accumulation with sub-grain level spatial resolution in a nickel-based polycrystal. In particular, with the combination of crystallographic orientation data and plastic strain measurements, the resolved shear strains on individual slip systems were spatially calculated across a substantial region of interest. W. Abuzaid et al. (2012a) measured plastic strain localization on individual slip systems on either side of the grain boundary and identified how these fields can be associated to the observed slip transfer. It is noted that our criterion is based on the local stress fields at the band tip, and

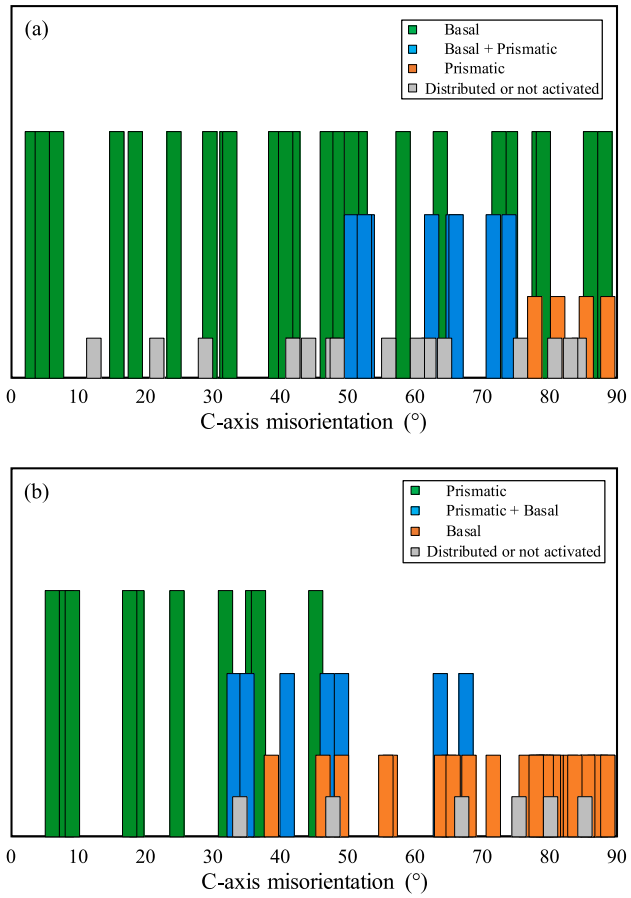

Fig. 17. Slip activity generated ahead of the slip band in the neighboring grain against the c-axis misorientation between two adjacent crystals for (a) basal, and (b) prismatic band type in Mg. Presented data suggests that when the misorientation is small, transmission to a like system is expected, while for high misorientations, slip in the parent grain is predicted to transmit onto an unlike system in the grain neighbor. The height of the bars has no physical meaning; the height differences are only used to distinguish the cases from one another.

not the strain fields. However, the condition of $RSS/SS > 1.0$ considered in the criterion to identify "activated" systems at the band tip confirms the plastic strain accumulation for those systems. Moreover, the concept of labeling slip activities at the band tip as "concentrated" or "distributed" can still be utilized if the shear strain on individual slip systems were available, instead of the resolved shear stresses.

6. Conclusions

In summary, we present a model built from the crystal plasticity FFT-based elasto-viscoplastic model to simulate the development of a crystallographic slip band spanning an HCP crystal. The technique, called SB-FFT, is employed to simulate the process of localization in a slip band. We consider intragranular slip bands that accumulate strain on either prismatic or basal slip planes and intersect the grain boundaries. The calculations include a full range of neighboring grain lattice orientations and a number of different HCP materials. In every case, the local stress fields that develop around and ahead of the slip band in the neighboring grain are analyzed. The main conclusions of this study are as follows:

- In HCP crystals, the lattice orientation of the nearest neighbor strongly affects the amount of plastic strain that localizes in the slip band.
- We show that neighbor orientations that respond to the slip band by activating plastically hard deformation modes facilitate slip band strain localization.
- Regardless of nearest neighbor orientation and crystallographic of the slip band, the levels of accumulated plastic strain in slip bands of the stronger CP-Ti are substantially greater than those in slip bands in Mg.
- A slip band tip stress-based criterion is proposed for identifying the nearest neighbor orientations in which slip band transmission is possible and the likely slip system onto which it occurs.

- Analysis of previously reported observations of slip to twin transmission suggest a local slip band tip stress-concentration criterion is a better indicator of a cross-GB transmission and the transmitted slip or twin system than conventionally used geometry-based factors.
- We show that for low GB misorientations, the slip band is likely to transmit into another slip band of the same type in the neighbor grain, while for high GB misorientations, it is likely to transmit into one of a different type or to not transmit at all.

Slip band stress concentrations can result in a number of additional instabilities, in both the parent and neighboring crystals. The SB-FFT method presented here can be used to study on the role of slip banding in slip band transmission across the boundary, and crack, twin, or void formation. The effects on the latter phenomenon can be investigated, for instance, via analysis of the stress triaxiality maps around and in front of the slip band (see examples in Appendix G).

Author statement

Behnam Ahmadikia: Conceptualization, Methodology, Formal analysis, Investigation, Visualization, Writing – original draft. M. Arul Kumar: Conceptualization, Methodology, Writing – review & editing, Funding acquisition. Irene Beyerlein: Conceptualization, Investigation, Writing – review & editing, Supervision, Funding acquisition.

Declaration of competing interest

The authors declare that they have no known competing financial interests or personal relationships that could have appeared to influence the work reported in this paper.

Acknowledgments

B. A. and I. J. B. gratefully acknowledge support by the National Science Foundation under Grant Number (1934641). M.A.K. acknowledges the financial support from the U.S. Department of Energy, Office of Basic Energy Sciences (OBES) FWP-06SCPE401.

Appendix A

To study the effect of the stress exponent (n) on the extent of strain localization within the slip band, the bi-crystal setup for which the evolution of localized shear is presented in Fig. 3 is selected and a set of simulations with different stress exponents have been conducted. In all simulations, the parent crystal has an orientation of $(90°, 90°, 45°)$ and the neighboring grain orientation is $(152°, 128°, 136°)$. Fig. A.1 Shows the average shear strain accumulated on the slip band system within the band domain ($\bar{\varepsilon}_{SB}$), normalized by that in the parent matrix ($\bar{\varepsilon}_{M}$), as the applied strain increases. It is found that a larger stress exponent yields a higher degree of strain localization in the slip band.

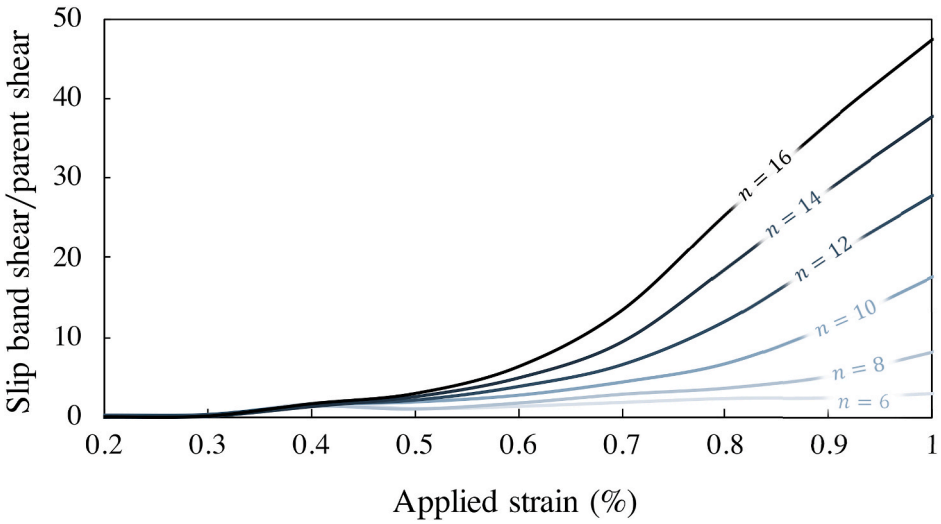

Fig. A.1. Average accumulated shear on the slip band system within the band domain normalized by that in the parent grain for different stress exponents exponent (n).

Appendix B

The overall plastic response of the neighboring grain depends on its orientation, i.e., the availability of its slip systems with respect to the far-field strain. As an illustration, Fig. B.1 shows the contours of equivalent plastic strain in the three typical cases of soft, moderate, and hard neighbor for CP-Ti bi-crystals subjected to 1% applied strain (properties of grain neighbor orientations for these three cases are listed in Table 2). As previously presented in Section 3.1., a harder neighbor promotes faster localization within the band. Furthermore, it is revealed that the neighbor in all three cases has undergone some plasticity, the extent of which varies from one case to another. Plastic strain in the soft neighbor is more uniformly distributed, while in the hard neighbor, it is developed mainly near the grain boundaries, especially at the slip band tip.

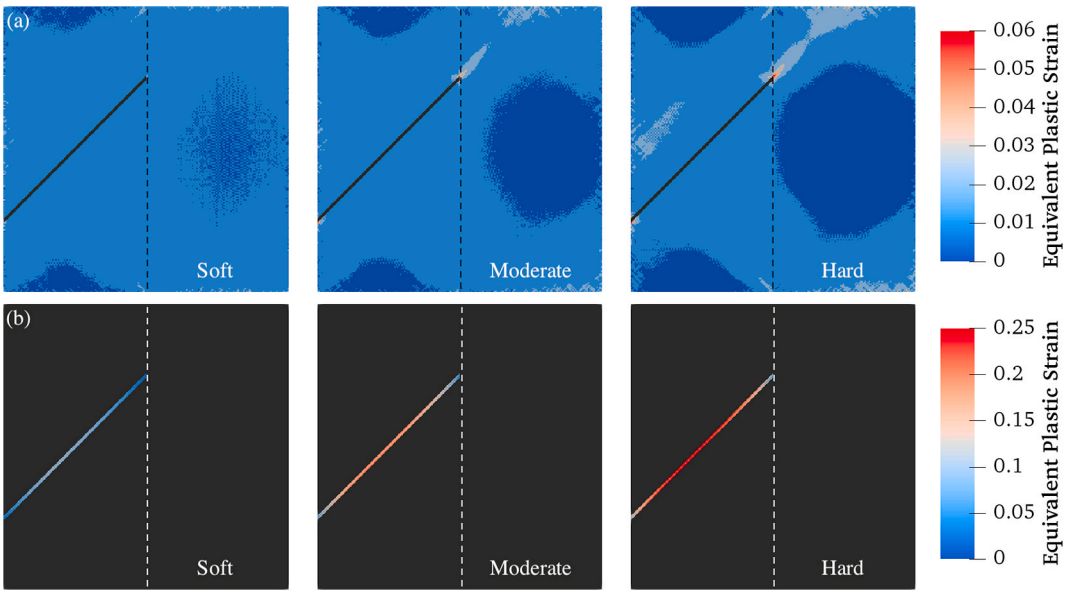

Fig. B.1. Distribution of the equivalent plastic strain in (a) parent and neighboring grains, and (b) slip band domain for three cases of soft, moderate, and hard neighbor in CP-Ti bi-crystals subjected to 1% macroscopic strain. Properties of grain neighbor orientations for these three cases are listed in Table 2. To represent the heterogeneity better, the slip band in (a) and the two grains in (b) are colored black.

Appendix C

Table C.1
Euler angles and the corresponding maximum Schmid factor of the easiest slip system for the neighboring grains that are excluded in Fig. 7(b).

$(138°,160°,66°)$	$(207°,137°,112°)$	$(39°,157°,343°)$	$(3°,93°,42°)$	$(145°,16°,169°)$	$(242°,168°,353°)$
$M_s = 0.23$	$M_s = 0.48$	$M_s = 0.25$	$M_s = 0.07$	$M_s = 0.22$	$M_s = 0.09$
$(121°,167°,16°)$	$(22°,92°,307°)$	$(58°,126°,266°)$	$(157°,163°,293°)$	$(20°,151°,92°)$	$(352°,146°,223°)$
$M_s = 0.11$	$M_s = 0.34$	$M_s = 0.39$	$M_s = 0.25$	$M_s = 0.37$	$M_s = 0.46$
$(26°,88°,163°)$	$(242°,13°,157°)$	$(12°,58°,81°)$	$(150°,4°,258°)$	$(353°,174°,254°)$	
$M_s = 0.37$	$M_s = 0.1$	$M_s = 0.45$	$M_s = 0.06$	$M_s = 0.09$	

Appendix D

To study the effect of elastic properties (e.g., elastic anisotropy) on strain localization within the slip band, in addition to CP-Ti and Mg which were studied in Fig. 7(a), degree of localization is investigated in a hypothetical material with plastic properties of CP-Ti and elastic properties of Mg. Fig. D.1 shows the average accumulated shear within the slip band normalized by that in the parent, for a broad range of neighbor orientations. Comparison of the results obtained for these three materials suggests that in addition to plastic properties (e.g., slip strength), elastic properties of HCP materials (e.g., elastic anisotropy) have an effect on strain localization within slip bands. Furthermore, plastic properties appear to have a stronger effect since the results for the hypothetical material are closer to those for CP-Ti than Mg.

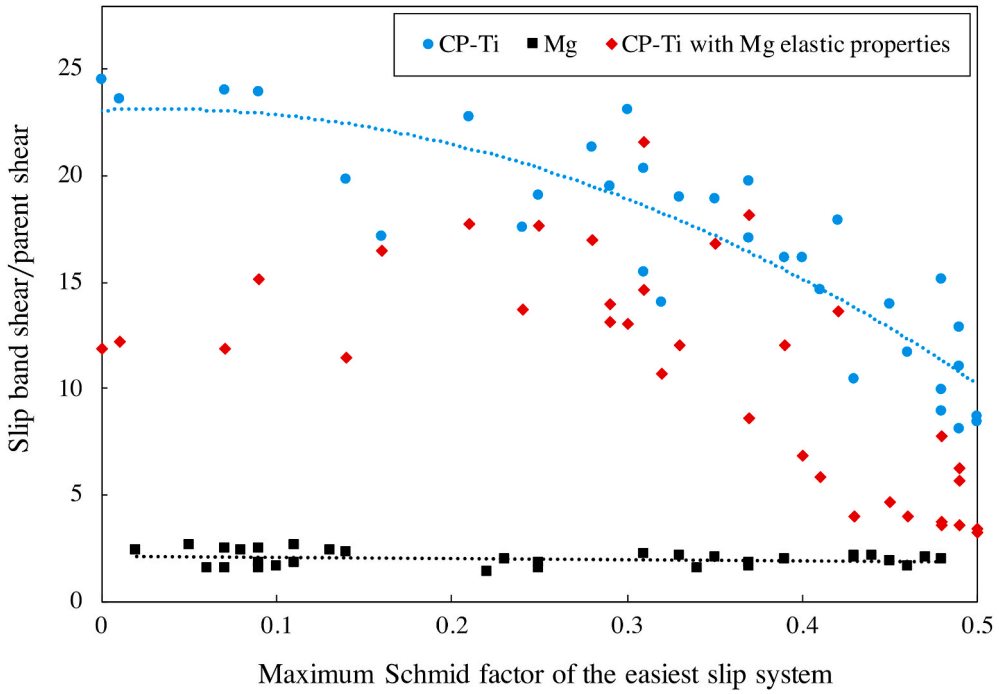

Fig. D.1. Average accumulated plastic strain on the slip band system within the slip band normalized by that in the parent grain for CP-Ti, Mg, and a hypothetical material with plastic properties of CP-Ti and elastic properties of Mg at 1% macroscopic applied strain for a broad range of grain neighbor orientations.

Appendix E

Fig. E.1 shows the extent of primary and secondary slip accumulated in the band domain for CP-Ti and Mg, each with a prismatic or basal slip band. The amount of slip is obtained at 1% applied strain and averaged over 50 different cases, each with a distinct neighbor orientation. Any slip occurred on a system other than slip band system is considered secondary slip. Fig. E.1 confirms that, especially for commonly observed situations of basal bands in Mg and prismatic bands in Ti, no significant secondary slip occurs in the band domain.

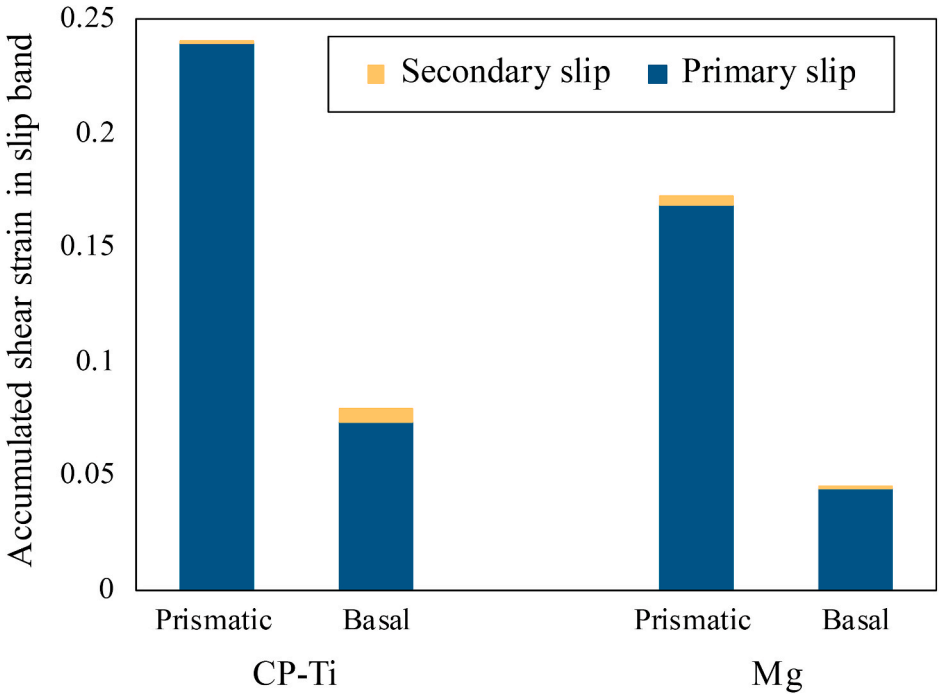

Fig. E.1. Extent of secondary slip accumulated within the band domain compared to the primary slip for CP-Ti and Mg with a prismatic/basal slip band subjected to 1% applied strain.

Appendix F

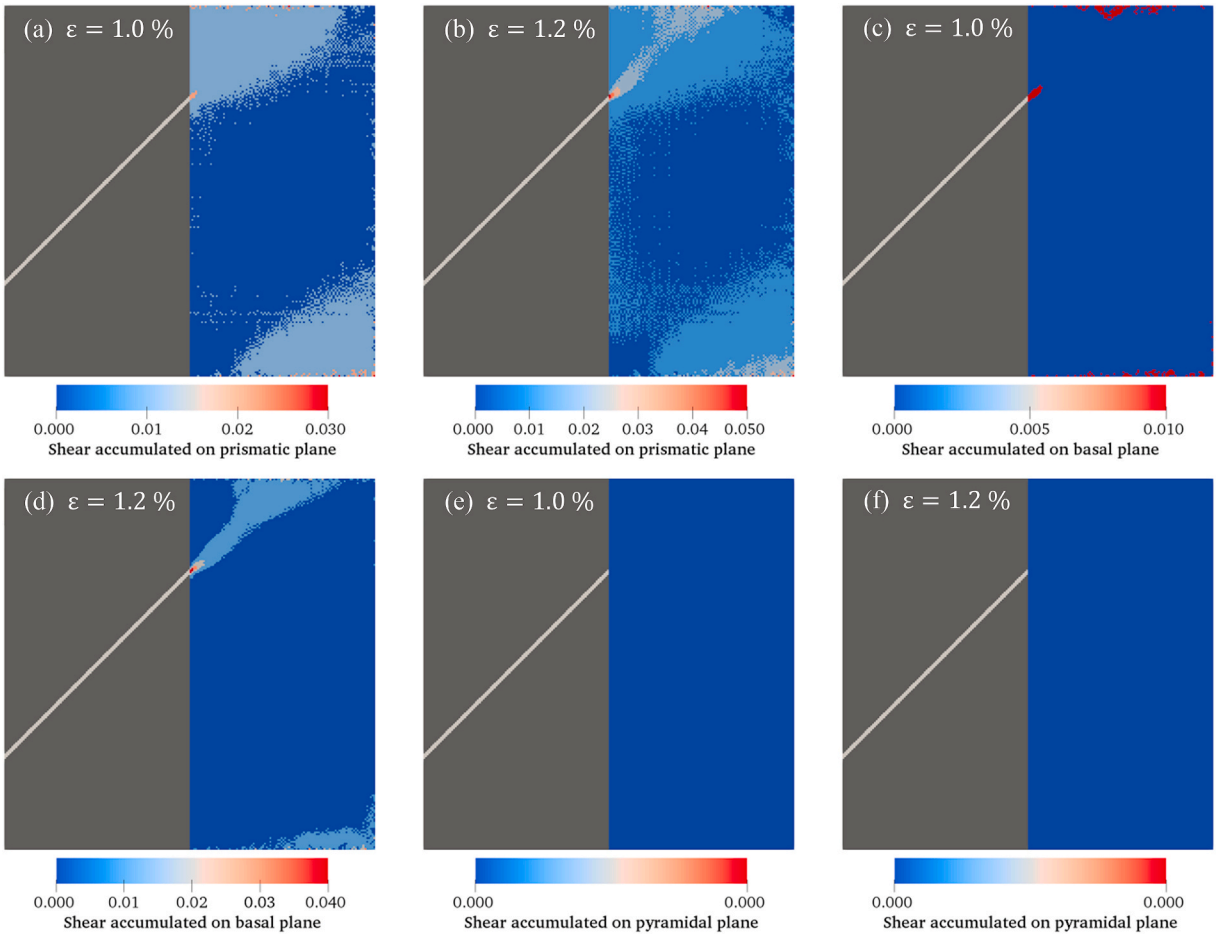

Fig. F.1. Accumulated shear strain for slip systems shown in Fig. 8; prismatic system at (a) 1% and (b) 1.2% applied strain, basal system at (c) 1% and (d) 1.2% applied strain, and pyramidal system at (e) 1% and (f) 1.2% applied strain.

Appendix G

Fig. G.1(a, b) shows the evolution of stress triaxiality within and around the slip band as the applied strain increases, respectively for a CP-Ti bi-crystal with a prismatic band and a Mg bi-crystal with a basal band. The Euler angles of the neighboring grain are $(22^\circ, 92^\circ, 307^\circ)$ in CP-Ti and $(12^\circ, 58^\circ, 81^\circ)$ in Mg. With the application of the far-field strain and as the slip band develops in CP-Ti, stress triaxiality in the parent grain starts to become nonuniformly distributed, such that within the band and in some areas around it, a larger triaxiality is formed. At 1% strain, nonuniformity of stress triaxiality is intensified. A strong triaxiality has developed at the intersection of the slip band and the grain boundary. Likewise, in the Mg bi-crystal, it is revealed that while some areas in the parent matrix experience a negative triaxiality, material points within the band domain manifest large positive stress triaxialities. While the degree of heterogeneity in and values of triaxiality around the slip band changes from one neighbor orientation to another, this observation holds true for all studied cases. Such increase in stress triaxiality around the band can have implications for formation of voids, especially at the band/GB intersection.

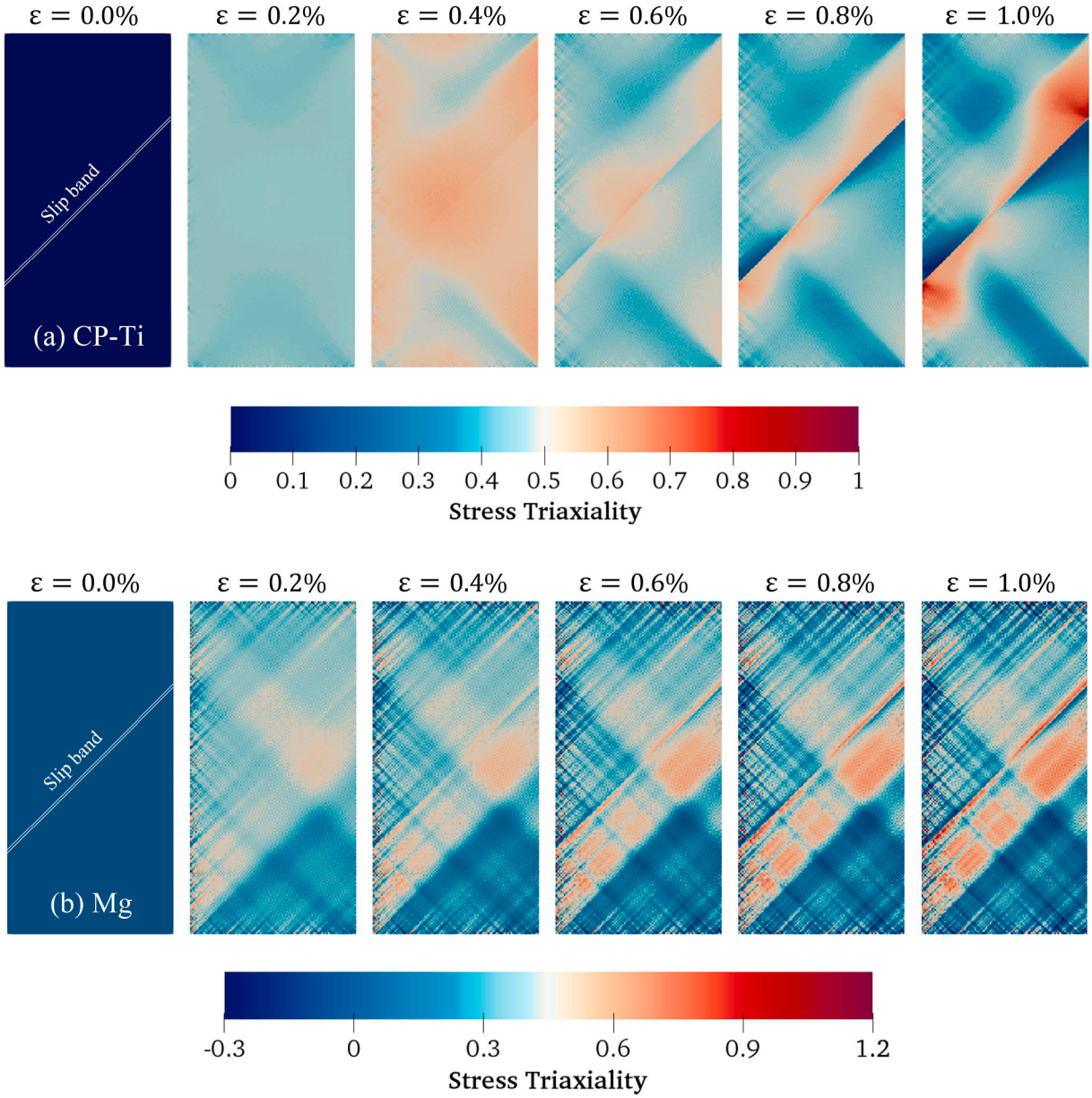

Fig. G.1. Distribution of stress triaxiality within and around the slip band as the applied strain increases, for (a) CP-Ti bi-crystal with a prismatic band, and (b) Mg bi-crystal with a basal band.

References

Abuzaid, W., Sangid, M.D., Sehitoglu, H., Carroll, J., Lambros, J., 2012a. The role of slip transmission on plastic strain accumulationacross grain boundaries. Procedia IUTAM 4, 169–178. https://doi.org/10.1016/j.piutam.2012.05.019.

Abuzaid, W.Z., Sangid, M.D., Carroll, J.D., Sehitoglu, H., Lambros, J., 2012b. Slip transfer and plastic strain accumulation across grain boundaries in Hastelloy X. J. Mech. Phys. Solid. 60, 1201–1220. https://doi.org/10.1016/j.jmps.2012.02.001.

Akhtar, A., Teghtsoonian, A., 1971. Plastic deformation of zirconium single crystals. Acta Metall. 19, 655–663. https://doi.org/10.1016/0001-6160(71)90019-8.

Alden, T.H., 1976. Microstructural interpretation of work softening in aluminum. Metallurgical Transactions A 7, 1057–1063. https://doi.org/10.1007/BF02656587.

Andani, M.T., Lakshmanan, A., Karamooz-Ravari, M., Sundararaghavan, V., Allison, J., Misra, A., 2020. A quantitative study of stress fields ahead of a slip band blocked by a grain boundary in unalloyed magnesium. Sci. Rep. 10, 1–8. https://doi.org/10.1038/s41598-020-59684-y.

Ardeljan, M., Knezevic, M., Nizolek, T., Beyerlein, I.J., Mara, N.A., Pollock, T.M., 2015. A study of microstructure-driven strain localizations in two-phase polycrystalline HCP/BCC composites using a multi-scale model. Int. J. Plast. 74, 35–57. https://doi.org/10.1016/j.ijplas.2015.06.003.

Armstrong, R.W., Ammon, H.L., Elban, W.L., Tsai, D.H., 2002. Investigation of hot spot characteristics in energetic crystals. Thermochim. Acta 384, 303–313. https://doi.org/10.1016/S0040-6031(01)00786-9.

Arsenlis, A., Parks, D.M., 2002. Modeling the evolution of crystallographic dislocation density in crystal plasticity. J. Mech. Phys. Solid. 50, 1979–2009. https://doi.org/10.1016/S0022-5096(01)00134-X.

Bapna, M.S., Meshii, M., 1974. Deformation of quench-hardened gold single crystals. Mater. Sci. Eng. 16, 181–191. https://doi.org/10.1016/0025-5416(74)90152-9.

Bapna, M.S., Mori, T., Meshii, M., 1968. The observation of slip channels in quenched gold. Phil. Mag.: J.Theor. Exp.Appl. Phys. 17, 177–184. https://doi.org/10.1080/14786436808218191.

Barton, N.R., Arsenlis, A., Marian, J., 2013. A polycrystal plasticity model of strain localization in irradiated iron. J. Mech. Phys. Solid. 61, 341–351. https://doi.org/10.1016/j.jmps.2012.10.009.

Barton, N.R., Dawson, P.R., 2001. On the spatial arrangement of lattice orientations in hot-rolled multiphase titanium. Model. Simulat. Mater. Sci. Eng. 9, 433. https://doi.org/10.1088/0965-0393/9/5/308.

Beyerlein, I.J., McCabe, R.J., Tomé, C.N., 2011. Effect of microstructure on the nucleation of deformation twins in polycrystalline high-purity magnesium: a multi-scale modeling study. J. Mech. Phys. Solid. 59, 988–1003. https://doi.org/10.1016/j.jmps.2011.02.007.

Bieler, T.R., Eisenlohr, P., Zhang, C., Phukan, H.J., Crimp, M.A., 2014. Grain boundaries and interfaces in slip transfer. Curr. Opin. Solid State Mater. Sci. 18, 212–226. https://doi.org/10.1016/j.cossms.2014.05.003.

Brechet, Y., Canova, G., Kubin, L.P., 1996. Strain softening, slip localization and propagation: from simulations to continuum modelling. Acta Mater. 44, 4261–4271. https://doi.org/10.1016/1359-6454(96)00115-2.

Bréchet, Y.J.M., Canova, G.R., Kubin, L.P., 1993. Static versus Propagative Plastic Strain Localizations. Scripta Metallurgica et Materialia, United States) 29. https://doi.org/10.1016/0956-716X(93)90103-Y.

Bridier, F., McDowell, D.L., Villechaise, P., Mendez, J., 2009. Crystal plasticity modeling of slip activity in Ti–6Al–4V under high cycle fatigue loading. Int. J. Plast. 25, 1066–1082. https://doi.org/10.1016/j.ijplas.2008.08.004.

Bridier, F., Villechaise, P., Mendez, J., 2005. Analysis of the different slip systems activated by tension in a α/β titanium alloy in relation with local crystallographic orientation. Acta Mater. 53, 555–567. https://doi.org/10.1016/j.actamat.2004.09.040.

Britton, T.B., Wilkinson, A.J., 2012. Stress fields and geometrically necessary dislocation density distributions near the head of a blocked slip band. Acta Mater. 60, 5773–5782. https://doi.org/10.1016/j.actamat.2012.07.004.

Busso, E.P., Meissonnier, F.T., O'dowd, N.P., 2000. Gradient-dependent deformation of two-phase single crystals. J. Mech. Phys. Solid. 48, 2333–2361. https://doi.org/10.1016/S0022-5096(00)00006-5.

Byun, T.S., Hashimoto, N., Farrell, K., Lee, E.H., 2006. Characteristics of microscopic strain localization in irradiated 316 stainless steels and pure vanadium. J. Nucl. Mater. 349, 251–264. https://doi.org/10.1016/j.jnucmat.2005.10.011.

Chan, K.S., Davidson, D.L., 1999. Evidence of void nucleation and growth on planar slip bands in a Nb-Cr-Ti alloy. Metall. Mater. Trans. 30, 579–585. https://doi.org/10.1007/s11661-999-0049-1.

Dai, L.H., Liu, L.F., Bai, Y.L., 2004. Formation of adiabatic shear band in metal matrix composites. Int. J. Solid Struct. 41, 5979–5993. https://doi.org/10.1016/j.ijsolstr.2004.05.023.

Diard, O., Leclercq, S., Rousselier, G., Cailletaud, G., 2005. Evaluation of finite element based analysis of 3D multicrystalline aggregates plasticity: application to crystal plasticity model identification and the study of stress and strain fields near grain boundaries. Int. J. Plast. 21, 691–722. https://doi.org/10.1016/j.ijplas.2004.05.017.

Ding, R., Gong, J., Wilkinson, A.J., Jones, I.P., 2016. A study of dislocation transmission through a grain boundary in hcp Ti–6Al using micro-cantilevers. Acta Mater. 103, 416–423. https://doi.org/10.1016/j.actamat.2015.10.023.

Dunne, F.P.E., Rugg, D., Walker, A., 2007. Lengthscale-dependent, elastically anisotropic, physically-based hcp crystal plasticity: application to cold-dwell fatigue in Ti alloys. Int. J. Plast. 23, 1061–1083. https://doi.org/10.1016/j.ijplas.2006.10.013.

Echlin, M.P., Stinville, J.C., Miller, V.M., Lenthe, W.C., Pollock, T.M., 2016. Incipient slip and long range plastic strain localization in microtextured Ti-6Al-4V titanium. Acta Mater. 114, 164–175. https://doi.org/10.1016/j.actamat.2016.04.057.

Eisenlohr, P., Diehl, M., Lebensohn, R.A., Roters, F., 2013. A spectral method solution to crystal elasto-viscoplasticity at finite strains. Int. J. Plast. 46, 37–53. https://doi.org/10.1016/j.ijplas.2012.09.012.

Erinosho, T.O., Dunne, F.P.E., 2015. Strain localization and failure in irradiated zircaloy with crystal plasticity. Int. J. Plast. 71, 170–194. https://doi.org/10.1016/j.ijplas.2015.05.008.

Estrin, Y., Kubin, L.P., 1986. Local strain hardening and nonuniformity of plastic deformation. Acta Metall. 34, 2455–2464. https://doi.org/10.1016/0001-6160(86)90148-3.

Forest, S., 1998. Modeling slip, kink and shear banding in classical and generalized single crystal plasticity. Acta Mater. 46, 3265–3281. https://doi.org/10.1016/S1359-6454(98)00012-3.

Guo, Y., Britton, T.B., Wilkinson, A.J., 2014. Slip band–grain boundary interactions in commercial-purity titanium. Acta Mater. 76, 1–12. https://doi.org/10.1016/j.actamat.2014.05.015.

Guo, Y., Collins, D.M., Tarleton, E., Hofmann, F., Wilkinson, A.J., Britton, T.B., 2020. Dislocation density distribution at slip band-grain boundary intersections. Acta Mater. 182, 172–183. https://doi.org/10.1016/j.actamat.2019.10.031.

Hagihara, K., Yokotani, N., Umakoshi, Y., 2010. Plastic deformation behavior of Mg12YZn with 18R long-period stacking ordered structure. Intermetallics 18, 267–276. https://doi.org/10.1016/j.intermet.2009.07.014.

Hirsch, P.B., Lally, J.S., 1965. The deformation of magnesium single crystals. Phil. Mag. 12, 595–648. https://doi.org/10.1080/14786436508218903.

Hure, J., El Shawish, S., Cizelj, L., Tanguy, B., 2016. Intergranular stress distributions in polycrystalline aggregates of irradiated stainless steel. J. Nucl. Mater. 476, 231–242. https://doi.org/10.1016/j.jnucmat.2016.04.017.

Kehagias, T., Komninou, P., Dimitrakopulos, G.P., Antonopoulos, J.G., Karakostas, T., 1995. Slip transfer across low-angle grain boundaries of deformed titanium. Scripta Metall. Mater. 33 https://doi.org/10.1016/0956-716X(95)00351-U.

Kube, C.M., 2016. Elastic anisotropy of crystals. AIP Adv. 6, 095209 https://doi.org/10.1063/1.4962996.

Kumar, M.A., Beyerlein, I.J., 2020. Local microstructure and micromechanical stress evolution during deformation twinning in hexagonal polycrystals. J. Mater. Res. 35, 217–241. https://doi.org/10.1557/jmr.2020.14.

Kumar, M.A., Beyerlein, I.J., Lebensohn, R.A., Tome, C.N., 2017. Role of alloying elements on twin growth and twin transmission in magnesium alloys. Mater. Sci. Eng., A 706, 295–303. https://doi.org/10.1016/j.msea.2017.08.084.

Kumar, M.A., Beyerlein, I.J., Tomé, C.N., 2016. Effect of local stress fields on twin characteristics in HCP metals. Acta Mater. 116, 143–154. https://doi.org/10.1016/j.actamat.2016.06.042.
Kumar, M.A., Hilairet, N., McCabe, R.J., Yu, T., Wang, Y., Beyerlein, I.J., Tomé, C.N., 2020. Role of twinning on the omega-phase transformation and stability in zirconium. Acta Mater. 185, 211–217. https://doi.org/10.1016/j.actamat.2019.12.006.
Lai, M.J., Tasan, C.C., Raabe, D., 2015. Deformation mechanism of ω-enriched Ti–Nb-based gum metal: dislocation channeling and deformation induced ω–β transformation. Acta Mater. 100, 290–300. https://doi.org/10.1016/j.actamat.2015.08.047.
Lebensohn, R.A., Brenner, R., Castelnau, O., Rollett, A.D., 2008. Orientation image-based micromechanical modelling of subgrain texture evolution in polycrystalline copper. Acta Mater. 56, 3914–3926. https://doi.org/10.1016/j.actamat.2008.04.016.
Lebensohn, R.A., Idiart, M.I., Castañeda, P.P., Vincent, P.-G., 2011. Dilatational viscoplasticity of polycrystalline solids with intergranular cavities. Phil. Mag. 91, 3038–3067. https://doi.org/10.1080/14786435.2011.561811.
Lebensohn, R.A., Kanjarla, A.K., Eisenlohr, P., 2012. An elasto-viscoplastic formulation based on fast Fourier transforms for the prediction of micromechanical fields in polycrystalline materials. Int. J. Plast. 32, 59–69. https://doi.org/10.1016/j.ijplas.2011.12.005.
Lebensohn, R.A., Needleman, A., 2016. Numerical implementation of non-local polycrystal plasticity using fast Fourier transforms. J. Mech. Phys. Solid. 97, 333–351. https://doi.org/10.1016/j.jmps.2016.03.023.
Lebensohn, R.A., Rollett, A.D., 2020. Spectral methods for full-field micromechanical modelling of polycrystalline materials. Comput. Mater. Sci. 173, 109336 https://doi.org/10.1016/j.commatsci.2019.109336.
Lee, T.C., Robertson, I.M., Birnbaum, H.K., 1990. TEM in situ deformation study of the interaction of lattice dislocations with grain boundaries in metals. Philos. Mag. A 62, 131–153. https://doi.org/10.1080/01418619008244340.
Lee, T.C., Robertson, I.M., Birnbaum, H.K., 1989. Prediction of slip transfer mechanisms across grain boundaries. Scripta Metall. 23, 799–803. https://doi.org/10.1016/0036-9748(89)90534-6.
Lentz, M., Risse, M., Schaefer, N., Reimers, W., Beyerlein, I.J., 2016. Strength and ductility with {10¯11}—{10¯12} double twinning in a magnesium alloy. Nat. Commun. 7, 1–7. https://doi.org/10.1038/ncomms11068.
Liu, B.-Y., Wang, J., Li, B., Lu, L., Zhang, X.-Y., Shan, Z.-W., Li, J., Jia, C.-L., Sun, J., Ma, E., 2014. Twinning-like lattice reorientation without a crystallographic twinning plane. Nat. Commun. 5, 1–6. https://doi.org/10.1038/ncomms4297.
Livingston, J.D., Chalmers, B., 1957. Multiple slip in bicrystal deformation. Acta Metall. 5, 322–327. https://doi.org/10.1016/0001-6160(57)90044-5.
Luster, J., Morris, M.A., 1995. Compatibility of deformation in two-phase Ti-Al alloys: dependence on microstructure and orientation relationships. Metall. Mater. Trans. 26, 1745–1756. https://doi.org/10.1007/BF02670762.
Marano, A., Gélébart, L., 2020. Non-linear composite voxels for FFT-based explicit modeling of slip bands: application to basal channeling in irradiated Zr alloys. Int. J. Solid Struct. https://doi.org/10.1016/j.ijsolstr.2020.04.027.
Marano, A., Gélébart, L., Forest, S., 2019. Intragranular localization induced by softening crystal plasticity: analysis of slip and kink bands localization modes from high resolution FFT-simulations results. Acta Mater. 175, 262–275. https://doi.org/10.1016/j.actamat.2019.06.010.
Melander, A., 1978. Work hardening and softening in a dislocation glide plane with precipitates. Mater. Sci. Eng. 34, 235–240. https://doi.org/10.1016/0025-5416(78)90055-1.
Montagnat, M., Castelnau, O., Bons, P.D., Faria, S.H., Gagliardini, O., Gillet-Chaulet, F., Grennerat, F., Griera, A., Lebensohn, R.A., Moulinec, H., 2014. Multiscale modeling of ice deformation behavior. J. Struct. Geol. 61, 78–108. https://doi.org/10.1016/j.jsg.2013.05.002.
Mori, T., Meshii, M., 1969. Plastic deformation of quench-hardened aluminum single crystals. Acta Metall. 17, 167–175. https://doi.org/10.1016/0001-6160(69)90137-0.
Nagra, J.S., Brahme, A., Lebensohn, R.A., Inal, K., 2017. Efficient fast Fourier transform-based numerical implementation to simulate large strain behavior of polycrystalline materials. Int. J. Plast. 98, 65–82. https://doi.org/10.1016/j.ijplas.2017.07.001.
Neeraj, T., Hou, D.-H., Daehn, G.S., Mills, M.J., 2000. Phenomenological and microstructural analysis of room temperature creep in titanium alloys. Acta Mater. 48, 1225–1238. https://doi.org/10.1016/S1359-6454(99)00426-7.
Neuhäuser, H., 1983. Slip-line formation and collective dislocation motion. Dislocations in solids 6, 319–440.
Niordson, C.F., Kysar, J.W., 2014. Computational strain gradient crystal plasticity. J. Mech. Phys. Solid. 62, 31–47. https://doi.org/10.1016/j.jmps.2013.08.014.
Olfe, J., Neuhäuser, H., 1988. Dislocation groups, multipoles, and friction stresses in α-CuZn alloys. Phys. Status Solidi 109, 149–160. https://doi.org/10.1002/pssa.2211090115.
Patra, A., McDowell, D.L., 2016. Crystal plasticity investigation of the microstructural factors influencing dislocation channeling in a model irradiated bcc material. Acta Mater. 110, 364–376. https://doi.org/10.1016/j.actamat.2016.03.041.
Patra, A., McDowell, D.L., 2013. Continuum modeling of localized deformation in irradiated bcc materials. J. Nucl. Mater. 432, 414–427. https://doi.org/10.1016/j.jnucmat.2012.08.021.
Patra, A., McDowell, D.L., 2012. Crystal plasticity-based constitutive modelling of irradiated bcc structures. Phil. Mag. 92, 861–887. https://doi.org/10.1080/14786435.2011.634855.
Rovinelli, A., Lebensohn, R.A., Sangid, M.D., 2015. Influence of microstructure variability on short crack behavior through postulated micromechanical short crack driving force metrics. Eng. Fract. Mech. 138, 265–288. https://doi.org/10.1016/j.engfracmech.2015.03.001.
Sauzay, M., Bavard, K., Karlsen, W., 2010. TEM observations and finite element modelling of channel deformation in pre-irradiated austenitic stainless steels–Interactions with free surfaces and grain boundaries. J. Nucl. Mater. 406, 152–165. https://doi.org/10.1016/j.jnucmat.2010.01.027.
Sharp, J.V., 1972. Correlation between cleared channels and surface slip steps in neutron irradiated copper crystals. Radiat. Eff. 14, 71–75. https://doi.org/10.1080/00337577208230474.
Shen, Z., Wagoner, R.H., Clark, W.A.T., 1986. Dislocation pile-up and grain boundary interactions in 304 stainless steel. Scripta Metall. 20, 921–926. https://doi.org/10.1016/0036-9748(86)90467-9.
Simmons, G., Wang, H., 1971. A Handbook of Single Crystal Elastic Constants and Calculated Aggregate Properties. MIT Press, Cambridge, MA, USA.
Sluys, L.J., Estrin, Y., 2000. The analysis of shear banding with a dislocation based gradient plasticity model. Int. J. Solid Struct. 37, 7127–7142. https://doi.org/10.1016/S0020-7683(99)00331-5.
Solas, D.E., Tomé, C.N., 2001. Texture and strain localization prediction using a N-site polycrystal model. Int. J. Plast. 17, 737–753. https://doi.org/10.1016/S0749-6419(00)00030-9.
Sweeney, C.A., Vorster, W., Leen, S.B., Sakurada, E., McHugh, P.E., Dunne, F.P.E., 2013. The role of elastic anisotropy, length scale and crystallographic slip in fatigue crack nucleation. J. Mech. Phys. Solid. 61, 1224–1240. https://doi.org/10.1016/j.jmps.2013.01.001.
Tatschl, A., Kolednik, O., 2003. On the experimental characterization of crystal plasticity in polycrystals. Mater. Sci. Eng., A 356, 447–463. https://doi.org/10.1016/S0921-5093(03)00095-9.
Ulmer, D.G., Altstetter, C.J., 1991. Hydrogen-induced strain localization and failure of austenitic stainless steels at high hydrogen concentrations. Acta Metall. Mater. 39, 1237–1248. https://doi.org/10.1016/0956-7151(91)90211-I.
Upadhyay, M.V., Capolungo, L., Taupin, V., Fressengeas, C., Lebensohn, R.A., 2016. A higher order elasto-viscoplastic model using fast fourier transforms: effects of lattice curvatures on mechanical response of nanocrystalline metals. Int. J. Plast. 83, 126–152. https://doi.org/10.1016/j.ijplas.2016.04.007.
Vasilev, E., Ferreri, N.C., Decker, R., Beyerlein, I.J., Knezevic, M., 2020. Strain-rate sensitivity, tension-compression asymmetry, r-ratio, twinning, and texture evolution of a rolled magnesium alloy Mg-1.3 Zn-0.4 Ca-0.4 Mn. Metall. Mater. Trans. 51, 3858–3868. https://doi.org/10.1007/s11661-020-05841-x.
Wang, J., Zecevic, M., Knezevic, M., Beyerlein, I.J., 2020. Polycrystal plasticity modeling for load reversals in commercially pure titanium. Int. J. Plast. 125, 294–313. https://doi.org/10.1016/j.ijplas.2019.09.013.
Wang, J., Wang, X., Yu, K., Rupert, T.J., Mahajan, S., Lavernia, E.J., Schoenung, J.M., Beyerlein, I.J., 2021. Manipulating deformation mechanisms with Y alloying of Mg. Mater. Sci. Eng. A. https://doi.org/10.1016/j.msea.2021.141373.

Wang, L., Yang, Y., Eisenlohr, P., Bieler, T.R., Crimp, M.A., Mason, D.E., 2010. Twin nucleation by slip transfer across grain boundaries in commercial purity titanium. Metall. Mater. Trans. 41, 421. https://doi.org/10.1007/s11661-009-0097-6.

Wang, L., Zheng, Z., Phukan, H., Kenesei, P., Park, J.-S., Lind, J., Suter, R.M., Bieler, T.R., 2017. Direct measurement of critical resolved shear stress of prismatic and basal slip in polycrystalline Ti using high energy X-ray diffraction microscopy. Acta Mater. 132, 598–610. https://doi.org/10.1016/j.actamat.2017.05.015.

Weidner, A., Beyer, R., Blochwitz, C., Holste, C., Schwab, A., Tirschler, W., 2006. Slip activity of persistent slip bands in polycrystalline nickel. Mater. Sci. Eng., A 435, 540–546. https://doi.org/10.1016/j.msea.2006.07.039.

Wejdemann, C., Pedersen, O.B., 2004. Atomic force microscopy of the intense slip localization causing fatigue crack initiation in polycrystalline brass. Mater. Sci. Eng., A 387, 556–559. https://doi.org/10.1016/j.msea.2003.12.095.

Williams, J.C., Baggerly, R.G., Paton, N.E., 2002. Deformation behavior of HCP Ti-Al alloy single crystals. Metall. Mater. Trans. 33, 837–850. https://doi.org/10.1007/s11661-002-0153-y.

Wronski, M., Kumar, M.A., Capolungo, L., McCabe, R.J., Wierzbanowski, K., Tome, C.N., 2018. Deformation behavior of CP-titanium: experiment and crystal plasticity modeling. Mater. Sci. Eng., A 724, 289–297. https://doi.org/10.1016/j.msea.2018.03.017.

Xiao, L., Umakoshi, Y., 2004. Cyclic deformation behavior and dislocation structure of Ti-2 at. Pct Al single crystals oriented for double prism slip. Metall. Mater. Trans. 35, 2845–2852. https://doi.org/10.1007/s11661-004-0232-3.

Xiao, L., Umakoshi, Y., 2003. Cyclic deformation behaviour and saturation bundle structure in Ti–5 at.% Al single crystals deforming by single prism slip. Phil. Mag. 83, 3407–3426. https://doi.org/10.1080/14786430310001603454.

Xiao, L., Umakoshi, Y., 2002. Cyclic deformation behaviour and dislocation structure of Ti-5 at.% Al single crystals oriented for double prism slip. Philos. Mag. A 82, 2379–2396. https://doi.org/10.1080/01418610208240042.

Xiao, X., Song, D., Xue, J., Chu, H., Duan, H., 2015. A size-dependent tensorial plasticity model for FCC single crystal with irradiation. Int. J. Plast. 65, 152–167. https://doi.org/10.1016/j.ijplas.2014.09.004.

Yoo, M.H., 1981. Slip, twinning, and fracture in hexagonal close-packed metals. Metallurgical transactions A 12, 409–418. https://doi.org/10.1007/BF02648537.

Zhang, M., Bridier, F., Villechaise, P., Mendez, J., McDowell, D.L., 2010. Simulation of slip band evolution in duplex Ti–6Al–4V. Acta Mater. 58, 1087–1096. https://doi.org/10.1016/j.actamat.2009.10.025.

Zhang, Z., Lunt, D., Abdolvand, H., Wilkinson, A.J., Preuss, M., Dunne, F.P., 2018. Quantitative investigation of micro slip and localization in polycrystalline materials under uniaxial tension. Int. J. Plast. 108, 88–106. https://doi.org/10.1016/j.ijplas.2018.04.014.

Zhang, Z.F., Wang, Z.G., 2003. Dependence of intergranular fatigue cracking on the interactions of persistent slip bands with grain boundaries. Acta Mater. 51, 347–364. https://doi.org/10.1016/S1359-6454(02)00399-3.

Zhou, B., Wang, L., Jin, P., Jia, H., Roven, H.J., Zeng, X., Li, Y., 2020. Revealing slip-induced extension twinning behaviors dominated by micro deformation in a magnesium alloy. Int. J. Plast. 128, 102669. https://doi.org/10.1016/j.ijplas.2020.102669.

Zhou, D., Moosbrugger, J.C., Morrison, D.J., 2006. Finite element simulation of PSB macroband nucleation and propagation in single crystal nickel cycled at low plastic strain amplitudes. Int. J. Plast. 22, 1336–1366. https://doi.org/10.1016/j.ijplas.2005.09.001.